Cell Reports

Article

Unique structural features govern the activity of a human mitochondrial AAA+ disaggregase, Skd3

Graphical abstract

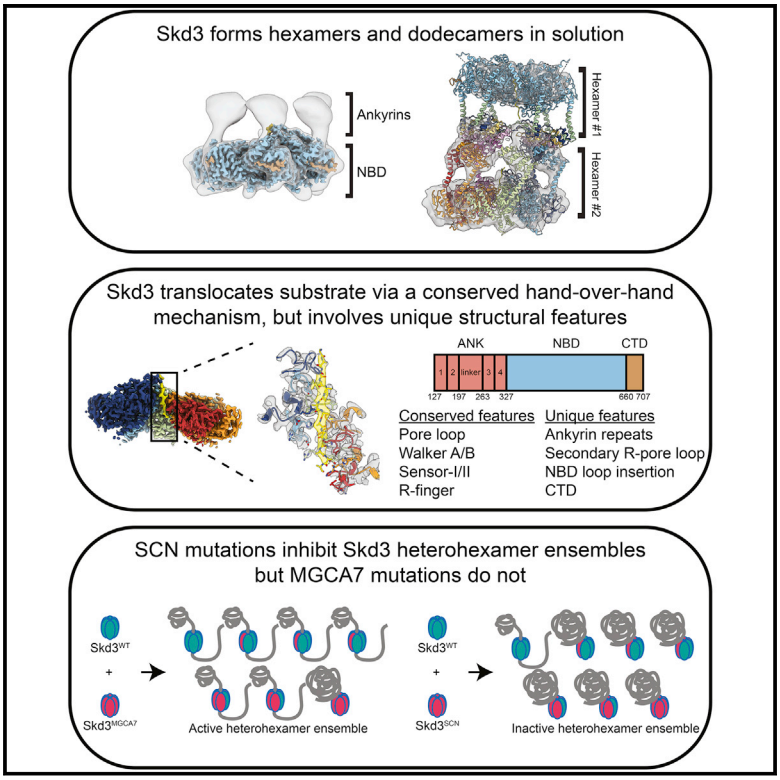

Highlights

- High-resolution structure of a $_{PARL}$Skd3-substrate complex
- Substrate-bound $_{PARL}$Skd3 hexamers stack head-to-head to form dodecamers
- Mechanisms by which $_{PARL}$Skd3 subunits collaborate to disaggregate proteins
- Mechanisms by which Skd3 mutations cause dominant and recessive forms of disease

Authors

Ryan R. Cupo, Alexandrea N. Rizo, Gabriel A. Braun, ..., Kushol Gupta, Daniel R. Southworth, James Shorter

Correspondence

daniel.southworth@ucsf.edu (D.R.S.), jshorter@pennmedicine.upenn.edu (J.S.)

In brief

Cupo et al. reveal the structure and mechanism of Skd3, a protein disaggregase found in mitochondria, which is critical for human health. These advances explain the inheritance patterns and suggest therapeutic strategies for debilitating diseases caused by mutations in Skd3.

Cupo et al., 2022, Cell Reports *40*, 111408
September 27, 2022
https://doi.org/10.1016/j.celrep.2022.111408

CellPress

Cell Reports

CellPress
OPEN ACCESS

Article

Unique structural features govern the activity of a human mitochondrial AAA+ disaggregase, Skd3

Ryan R. Cupo,[1,2,6] Alexandrea N. Rizo,[3,4,6] Gabriel A. Braun,[5] Eric Tse,[3] Edward Chuang,[1,2] Kushol Gupta,[1] Daniel R. Southworth,[3,7,*] and James Shorter[1,2,7,8,*]

[1]Department of Biochemistry and Biophysics, University of Pennsylvania, Philadelphia, PA, USA
[2]Pharmacology Graduate Group, Perelman School of Medicine, University of Pennsylvania, Philadelphia, PA, USA
[3]Department of Biochemistry and Biophysics, University of California, San Francisco, San Francisco, CA, USA
[4]Graduate Program in Chemical Biology, University of Michigan, Ann Arbor, MI, USA
[5]Chemistry and Chemical Biology Graduate Program, Institute for Neurodegenerative Diseases, University of California, San Francisco, San Francisco, CA, USA
[6]These authors contributed equally
[7]Senior author
[8]Lead contact
*Correspondence: daniel.southworth@ucsf.edu (D.R.S.), jshorter@pennmedicine.upenn.edu (J.S.)
https://doi.org/10.1016/j.celrep.2022.111408

SUMMARY

The AAA+ protein, Skd3 (human *CLPB*), solubilizes proteins in the mitochondrial intermembrane space, which is critical for human health. Skd3 variants with defective protein-disaggregase activity cause severe congenital neutropenia (SCN) and 3-methylglutaconic aciduria type 7 (MGCA7). How Skd3 disaggregates proteins remains poorly understood. Here, we report a high-resolution structure of a Skd3-substrate complex. Skd3 adopts a spiral hexameric arrangement that engages substrate via pore-loop interactions in the nucleotide-binding domain (NBD). Substrate-bound Skd3 hexamers stack head-to-head via unique, adaptable ankyrin-repeat domain (ANK)-mediated interactions to form dodecamers. Deleting the ANK linker region reduces dodecamerization and disaggregase activity. We elucidate apomorphic features of the Skd3 NBD and C-terminal domain that regulate disaggregase activity. We also define how Skd3 subunits collaborate to disaggregate proteins. Importantly, SCN-linked subunits sharply inhibit disaggregase activity, whereas MGCA7-linked subunits do not. These advances illuminate Skd3 structure and mechanism, explain SCN and MGCA7 inheritance patterns, and suggest therapeutic strategies.

INTRODUCTION

Protein aggregation and aberrant phase transitions can be deleterious. Thus, specialized protein disaggregases have evolved to safely reverse protein aggregation and restore resolubilized proteins to native form and function (Fare and Shorter, 2021). These include ATP-independent systems, such as DAXX, TRIMs, and nuclear-import receptors, as well as ATP-dependent systems, including specific AAA+ (ATPases associated with diverse cellular activities) proteins, such as Hsp104 and Skd3 (human *CLPB*) (Cupo and Shorter, 2020b; Fare and Shorter, 2021; Huang et al., 2021; Zhu et al., 2020).

AAA+ proteins couple ATP hydrolysis to mechanical work to drive energetically challenging tasks, including protein disaggregation (Puchades et al., 2020). Thus, Hsp104, a hexameric, double AAA+ ring disaggregase found in all non-metazoan eukaryotes, disassembles stable cross-β structures, disordered aggregates, toxic oligomers, and heat-induced condensates (DeSantis et al., 2012; Shorter and Southworth, 2019; Yoo et al., 2022). To disaggregate proteins, Hsp104 translocates polypeptides into its central channel using tyrosine-bearing pore loops that grip the substrate (Shorter and Southworth, 2019). Curiously, despite conferring neuroprotection when expressed in animals (Cushman-Nick et al., 2013; Lo Bianco et al., 2008), Hsp104 was lost during the transition from protozoa to metazoa, as was its mitochondrial counterpart, Hsp78 (Erives and Fassler, 2015). However, humans express Skd3 (human *CLPB*), a single AAA+ ring disaggregase found in the mitochondrial intermembrane space (IMS) (Antonicka et al., 2020; Botham et al., 2019; Hung et al., 2014; Rath et al., 2021; Rhee et al., 2013; Thevarajan et al., 2020), which first appears in evolution alongside Hsp104 and Hsp78 in the closest extant protozoan relatives of animals (Erives and Fassler, 2015). Skd3 is related to Hsp104 and Hsp78 via its HCLR clade AAA+ domain, but otherwise shares limited homology (Cupo and Shorter, 2020b; Erives and Fassler, 2015; Erzberger and Berger, 2006; Perier et al., 1995).

Skd3 maintains protein solubility in the IMS to ensure mitochondrial functionality (Chen et al., 2019; Cupo and Shorter, 2020b; Warren et al., 2022). Skd3 exhibits potent protein-disaggregase activity and is critical for human health (Cupo and

Shorter, 2020b; Warren et al., 2022). Autosomal dominant mutations in Skd3 that impair disaggregase activity cause severe congenital neutropenia (SCN) (Warren et al., 2022). SCN is a rare bone marrow failure syndrome that presents with impaired neutrophil maturation (Skokowa et al., 2017). Due to low neutrophil counts, SCN patients are prone to life-threatening infections, myelodysplastic syndromes, and acute myeloid leukemia (Skokowa et al., 2017). By contrast, autosomal recessive or distinct biallelic mutations in Skd3 that impair disaggregase activity underlie 3-methylglutaconic aciduria type 7 (MGCA7) (Cupo and Shorter, 2020b; Kanabus et al., 2015; Kiykim et al., 2016; Pronicka et al., 2017; Saunders et al., 2015; Wortmann et al., 2015, 2021). MGCA7 presents with elevated levels of 3-methylglutaconic acid, neurologic deterioration, and neutropenia (Wortmann et al., 2015). In severe cases, patients present with infantile onset of progressive encephalopathy with movement abnormalities and delayed psychomotor development, which can be accompanied by cataracts, seizures, recurrent infections, and death a few weeks after birth (Wortmann et al., 2015). There are no effective therapeutics for severe MGCA7.

Despite the importance of Skd3 for human health, little is known about Skd3 mechanism or structure (Cupo and Shorter, 2020b). Skd3 harbors an N-terminal mitochondrial targeting signal, which is cleaved by mitochondrial processing peptidase upon import into mitochondria (Wortmann et al., 2015). Skd3 then has an autoinhibitory hydrophobic peptide, which is removed by PARL, a rhomboid protease in the mitochondrial inner membrane (Saita et al., 2017; Spinazzi et al., 2019). Removal of this peptide increases Skd3 disaggregase activity by more than 10-fold (Cupo and Shorter, 2020b). Thus, Skd3 is only fully activated upon reaching its final destination in the IMS. After these processing events, the mature form of Skd3 contains an ankyrin-repeat domain (ANK), a nucleotide-binding domain (NBD) from the HCLR clade of the AAA+ family, and a short C-terminal domain (CTD) (Figure 1A).

The ANK-AAA+ domain combination is an unusual feature of Skd3. Both the ANK and NBD are required for Skd3 disaggregase activity as deletion of either domain ablates activity (Cupo and Shorter, 2020b). How the ANK and NBD collaborate to power disaggregation is unknown. The ANK is comprised of two ankyrin repeats, a linker, and two more ankyrin repeats (Figure 1A). Ankyrin repeats adopt a helix-turn-helix conformation, which can enable specific protein-protein interactions (Kohl et al., 2003; Mosavi et al., 2004; Parra et al., 2015). Intriguingly, ankyrin repeats are a core component of an ATP-independent disaggregase, cpSRP43 (Jaru-Ampornpan et al., 2010, 2013). The Skd3 NBD is homologous to NBD2 of Hsp104 and bacterial ClpB (Cupo and Shorter, 2020b). Like Hsp104, Skd3 couples ATP hydrolysis to protein disaggregation, which requires conserved AAA+ motifs, such as Walker A, Walker B, and pore-loop tyrosines (Cupo and Shorter, 2020b). However, the Skd3 NBD contains an apomorphic insertion at residues L507–I534 that is not observed in any other AAA+ protein (Cupo and Shorter, 2020b). What role this insertion plays in Skd3 activity is unknown. Skd3 has an extended CTD that is patterned with acidic and basic residues (Cupo and Shorter, 2020b). By contrast, *S. cerevisiae* Hsp104 has an extended, acidic CTD that contributes to hexamerization (Mackay et al., 2008). How the CTD contributes to Skd3 function is unknown.

SCN-linked mutations in Skd3 cluster in the NBD (Warren et al., 2022), whereas biallelic MGCA-7-linked mutations are scattered throughout Skd3 (Wortmann et al., 2015). SCN-linked mutations impair ATPase and disaggregase activity (Warren et al., 2022). MGCA7-linked mutations impair disaggregase activity in a manner that predicts disease severity (Cupo and Shorter, 2020b). However, MGCA7-linked mutations do not always impair ATPase activity (Cupo and Shorter, 2020b). It is not understood why SCN-linked mutations are dominant-negative, whereas MGCA7-linked mutations are recessive.

It is often assumed that Skd3 structure and mechanism closely resemble that of Hsp104/ClpB (Capo-Chichi et al., 2015; Kanabus et al., 2015; Saunders et al., 2015). Yet, there are few studies of Skd3 disaggregase activity (Cupo and Shorter, 2020b; Mroz et al., 2020; Warren et al., 2022; Wortmann et al., 2021). Unlike Hsp104/ClpB, Skd3 does not require Hsp70 or Hsp40 to disaggregate disordered aggregates (Cupo and Shorter, 2020b). Moreover, Skd3 shares only ~20% sequence identity with Hsp104/ClpB and has only one domain, the NBD, in common with Hsp104/ClpB (Cupo and Shorter, 2020b; Erives and Fassler, 2015). Here, we employ cryoelectron microscopy (cryo-EM) and biochemical reconstitution to reveal Skd3 structure and mechanism.

RESULTS

$_{PARL}$Skd3 structure reveals a substrate-bound AAA+ spiral and flexible ANKs

To capture a substrate-bound state of Skd3, we included a model substrate casein, which binds to wild-type (WT) PARL-protease-activated Skd3 ($_{PARL}$Skd3; Figure 1A) (Cupo and Shorter, 2020b). $_{PARL}$Skd3 binding to FITC-labeled casein was assessed under different nucleotide conditions (Figure S1A). Binding was detected under all conditions, but $_{PARL}$Skd3 bound FITC-casein more effectively in the presence of non-hydrolyzable AMP-PNP (K_D ~ 0.1 μM), ATP (K_D ~ 0.5 μM), or slowly hydrolyzable ATPγS (K_D ~ 0.4 μM) in contrast to ADP or no nucleotide (Figure S1A). Thus, $_{PARL}$Skd3 differs from Hsp104, where only ATPγS facilitates avid polypeptide binding (Gates et al., 2017; Weaver et al., 2017).

We assessed the oligomeric state of $_{PARL}$Skd3 by size-exclusion chromatography (SEC) (Figures 1B and S1B–S1D). Following incubation with ATPγS, AMP-PNP, or ADP without FITC-casein substrate, $_{PARL}$Skd3 exhibits a broad elution profile with peaks likely corresponding to dodecamers (792 kDa), hexamers (396 kDa), smaller oligomers, and monomers (66 kDa; Figure S1B). By contrast, in the presence of FITC-casein, $_{PARL}$Skd3 shifted toward dodecamers in all nucleotide conditions (Figures 1B and S1C). Thus, substrate binding by $_{PARL}$Skd3 promotes dodecamerization. Indeed, it has been independently established that $_{PARL}$Skd3 forms dodecamers (Spaulding et al., 2022; Wu et al., 2022). Moreover, Skd3 forms higher-order structures in cells, consistent with dodecamer formation (Thevarajan et al., 2020).

Previously, we used ATPγS to stabilize substrate-bound states of Hsp104/ClpB (Gates et al., 2017; Rizo et al., 2019).

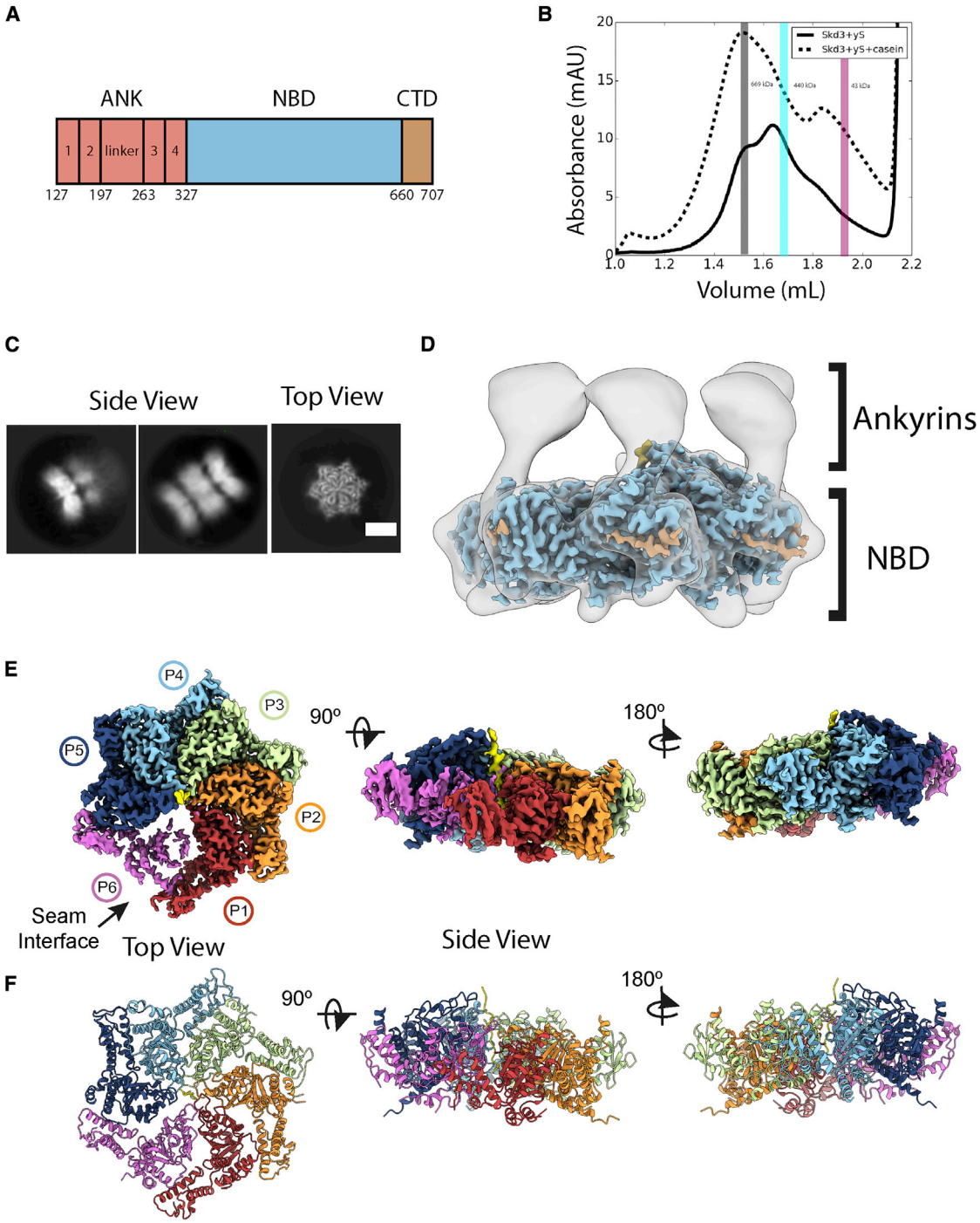

Figure 1. Structure of $_{PARL}$Skd3

(A) $_{PARL}$Skd3 domain architecture.

(B) SEC of $_{PARL}$Skd3 incubated with ATPγS (solid) or ATPγS and FITC-casein (dashed). Vertical bars indicate molecular weight standards: thyroglobulin (669 kDa), ferritin (440 kDa), and ovalbumin (43 kDa), and are representative of $_{PARL}$Skd3 dodecamer (gray), hexamer (cyan), or monomer (magenta) size. The gray bar also represents the fraction taken for cryo-EM analysis of $_{PARL}$Skd3:casein.

(C) Cryo-EM 2D class averages of the $_{PARL}$Skd3:casein:ATPγS complex showing representative side (left) and top (right) views. Scale bar, 100 Å.

(D) Overlay of low-pass filtered hexamer map and high-resolution sharpened map colored by domain as in (A).

(E and F) (E) Final 2.9-Å-resolution sharpened map and (F) molecular model colored by individual protomers (P1–P6), with substrate polypeptide (yellow) in the channel. See also Figures S1 and S2 and Video S1.

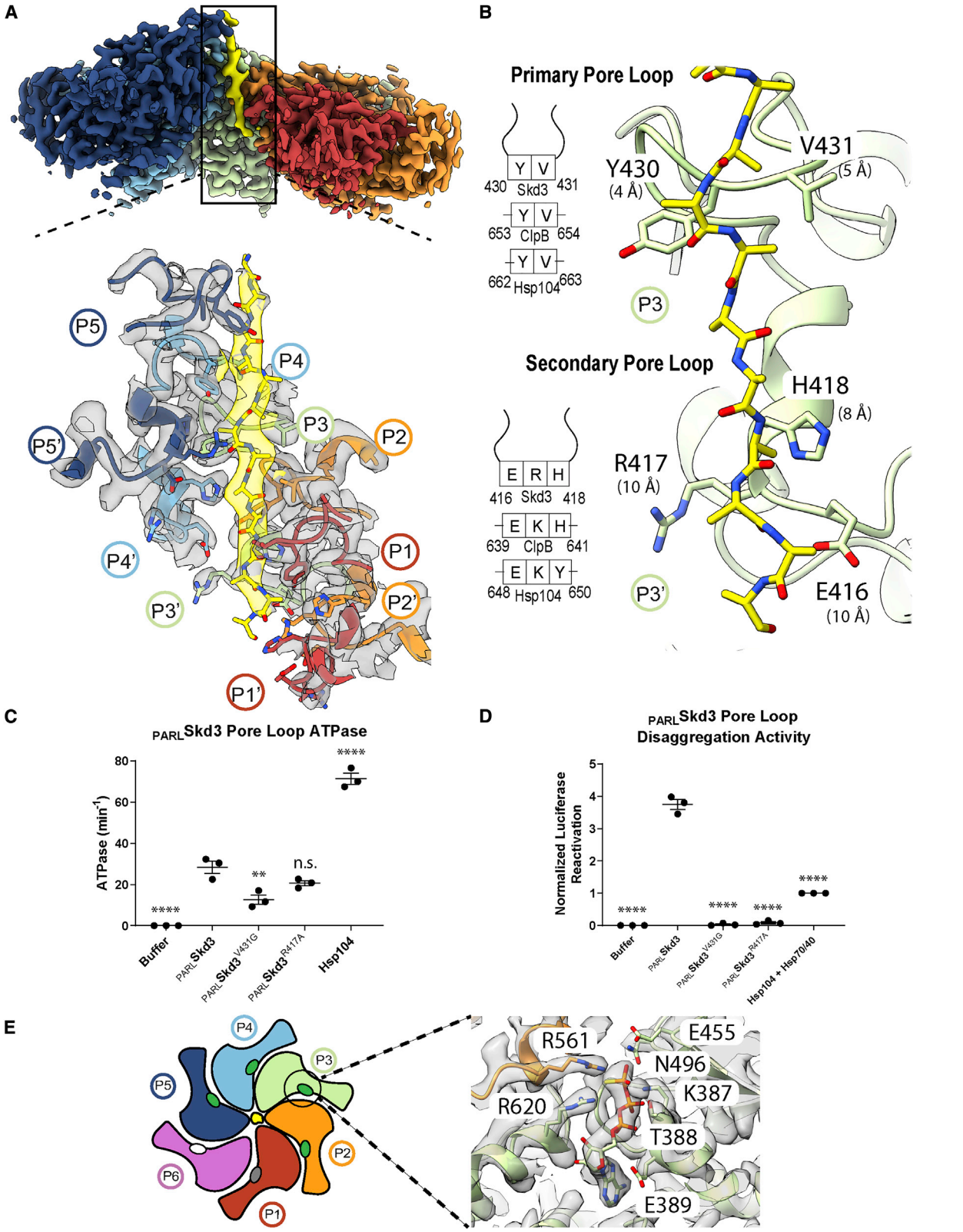

(legend on next page)

SEC-purified $_{PARL}$Skd3:casein forms stable complexes in the presence of ATPγS (Figures 1C and S1E). Reference-free 2D class averages show a variety of top and side views with well-resolved features (Figures 1C and S1E). Top views revealed two particle classes: a major class with a hexameric ring containing density in the central channel, and a minor class with a heptameric ring and an empty channel (Figure S1E). Top views of the hexameric ring appeared similar to substrate-bound Hsp104/ClpB (Gates et al., 2017; Rizo et al., 2019), whereas side views revealed a distinct arrangement with two or three bands of density, indicating a stacked-ring arrangement of the $_{PARL}$Skd3:casein complex (Figures 1C and S1E). Notably, side views exhibit one strong band of density with well-resolved features, whereas the other bands are more diffuse, indicating flexibility or differential occupancy (Figure 1C).

Following 3D classification with four classes, we identified three distinct oligomeric arrangements: a hexameric double-ring complex that contains density in the channel (class 1), a hexameric three-ring complex that contains density in the central channel for one well-resolved ring (class 2), and a heptameric form containing two rings and an empty central channel (class 3) (Figure S1F). Given the low abundance of the heptameric ring and the absence of density for substrate, class 3 was not pursued further. Class 1 had the highest percentage of particles (41%) and a well-defined AAA+ ring. Thus, refinement was performed with class 1, resulting in a final resolution of 2.9Å for the $_{PARL}$Skd3:casein complex (Figures S2A–2H; Table S1; Video S1). A molecular model for the hexameric ring comprised of the NBD, which refined to the highest resolution (~2.5 Å) in the map (Figure S2E), was determined using homology models generated by SWISS-Model (Waterhouse et al., 2018).

At an increased threshold, lower-resolution density extends from the N-terminal end of the NBDs and forms a second ring of separated and flexible globular structures (Figure 1D). These separated regions contrast with the extensive contact interfaces of the NBDs in the AAA+ ring (Figure 1D). Based on the molecular model of the NBDs and the position of the N-terminal AAA+ residues, we conclude that these separated regions are the N-terminal ANKs (Figures 1A and 1D). Given this architecture for a hexameric arrangement, we propose that the three-ring structures identified in the 2D class averages and in class 2 in the 3D classification are dodecamers comprised of two $_{PARL}$Skd3 hexamers that interact via the ANKs, which form the middle ring of density (Figures 1C and S1F). Considering the flexibility of the ANKs and the second AAA+ ring, we postulate that, in addition to the hexamer form, class 1 likely contains dodecamers in which the second ring is poorly aligned and not visible in the reconstruction due to its flexibility. Indeed, when 2D classification of the class 1 particle is performed, weak density for a second AAA+ ring is identified in many side-view class averages, indicating a dodecamer (Figure S2A). Furthermore, SEC in tandem with multi-angle light scattering confirms $_{PARL}$Skd3 dodecamers in solution (Figure S1G). We suggest that the active, substrate-bound form of $_{PARL}$Skd3 likely exists in a dynamic equilibrium between hexamers and dodecamers.

The $_{PARL}$Skd3 NBDs adopt a right-handed spiral, wherein five protomers directly contact substrate polypeptide along a 40-Å-length of the channel (Figures 1E and 1F;, Video S1). These well-resolved protomers (P1–P5) are positioned in a helical arrangement, each with a rise of ~6 Å and rotation of ~60° along the substrate. Protomer P6 is at the seam interface between the lowest (P1) and highest (P5) substrate contact sites but is disconnected and has lower resolution, resulting in an asymmetric position within the spiral (Figures 1E and 1F). This architecture is akin to other substrate-bound AAA+ structures, including Hsp104/ClpB (Gates et al., 2017; Rizo et al., 2019). Additional density is identified in protomers P3–P5 that extend from the small sub-domain of the NBD toward the adjacent clockwise protomer, and is likely the CTD (Figure 1D).

Substrate contacts and NBD occupancy support a conserved, stepwise translocation model

Pore loop-substrate interactions and nucleotide states in the $_{PARL}$Skd3 hexamer structure suggest a translocation mechanism. An extended polypeptide is well resolved in the $_{PARL}$Skd3 channel and modeled as a 14-residue polyA peptide (Figure 2A). Based on previous work (Gates et al., 2017; Lopez et al., 2020; Rizo et al., 2019) and binding data (Figures S1A and S1D), we conclude that this extended polypeptide is a nonspecific portion of FITC-casein. The canonical pore loops (residues 429–432) for protomers P1–P5 directly bind the substrate backbone via a conserved YV motif (Y430 and V431; Figures 2A and 2B). These pore loops form a spiral staircase of contacts and comprise the primary substrate-binding sites identified in the structure, supporting their established role in translocase function (Shorter and Southworth, 2019). Indeed, mutation of the conserved tyrosine to alanine (Y430A) reduces ATPase activity and abolishes disaggregase activity (Cupo and Shorter, 2020b). We now find

Figure 2. Spiral of pore loop-substrate contacts and nucleotide states of $_{PARL}$Skd3

(A) Cryo-EM density map (top) of protomers (P1–P5) and substrate (yellow) and expanded view (bottom) of the channel, including the primary (P1–P5) and secondary (P1′–P5′) loops interacting in a spiral along the 14-residue substrate strand. P1 is the canonical pore loop from protomer 1 and P1′ is the secondary pore loop from protomer 1.

(B) The primary and secondary pore loop-substrate contacts for P4, including distances to substrate (measured between α-carbons) and a schematic indicating conservation with Hsp104/ClpB.

(C) ATPase activity of $_{PARL}$Skd3, $_{PARL}$Skd3^{V431G}, $_{PARL}$Skd3^{R417A}, and Hsp104. ATPase activity was compared with $_{PARL}$Skd3 using one-way ANOVA and a Dunnett's multiple comparisons test (n = 3, individual data points shown as dots, bars show mean ± SEM, **p < 0.01, ****p < 0.0001).

(D) Luciferase disaggregase activity of $_{PARL}$Skd3, $_{PARL}$Skd3^{V431G}, $_{PARL}$Skd3^{R417A}, and Hsp104 plus Hsp70 and Hsp40. Luciferase activity was normalized to Hsp104 plus Hsp70 and Hsp40. Disaggregase activity was compared with $_{PARL}$Skd3 using one-way ANOVA and a Dunnett's multiple comparisons test (n = 3, individual data points shown as dots, bars show mean ± SEM, ****p < 0.0001).

(E) Schematic indicating nucleotide states (ovals) for each protomer (ATP, green; ADP, gray; apo, white) and expanded view of P4 nucleotide-binding pocket showing density for ATP and conserved interacting residues, including Arg finger (R561), sensor-1 (N496), sensor-2 (R620), Walker A (K387), and Walker B (E455). See also Figure S2 and Video S1.

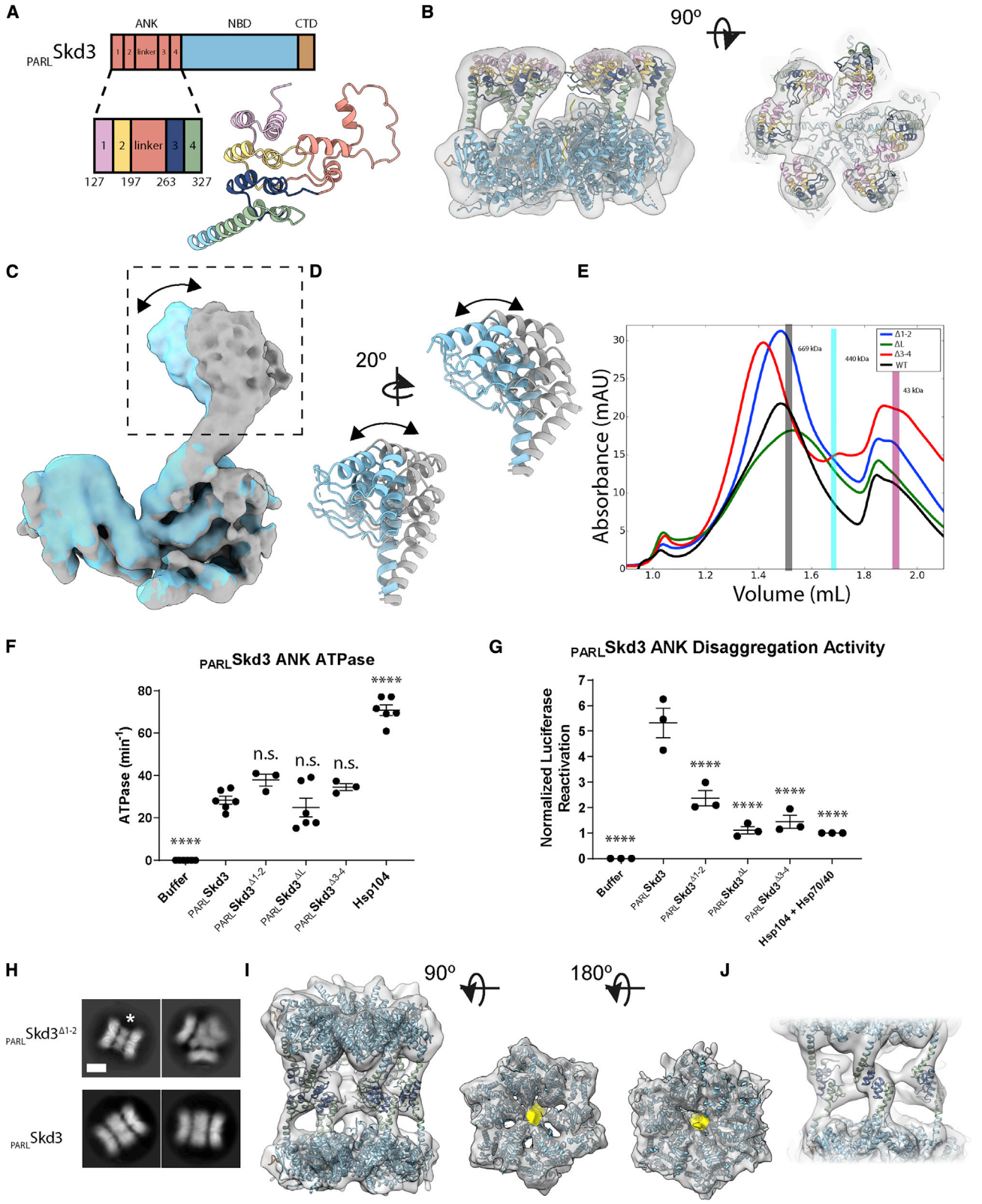

(legend on next page)

that V431G also reduces $_{PARL}$Skd3 ATPase activity and abolishes disaggregase activity (Figures 2C and 2D). These results are consistent with our $_{PARL}$Skd3 structure where Y430 and V431 directly engage substrate.

An additional spiral of substrate interactions at the channel exit is formed by secondary pore-loop motifs from protomers P2–P5 (Figures 2A and 2B). In $_{PARL}$Skd3, residues E416, R417, and H418 comprise this secondary pore loop, which is positioned in line with canonical YV loops above, but slightly further away (~9 Å) from the substrate backbone (Figures 2A and 2B). To define the role of the secondary pore loop, we generated $_{PARL}$Skd3^{R417A}, which exhibited similar ATPase activity to $_{PARL}$Skd3 (Figure 2C), but diminished disaggregase activity (Figure 2D). This loss of function is much more severe than that caused by equivalent mutations in Hsp104/ClpB (Howard et al., 2020; Rizo et al., 2019). Thus, the secondary pore loops play a more critical role in $_{PARL}$Skd3 disaggregase activity than in Hsp104/ClpB.

The nucleotide-binding pockets in substrate-bound $_{PARL}$Skd3 are positioned at inter-protomer interfaces with conserved AAA+ residues contacting the nucleotide (Figures 2E and S2I). For protomers P2–P5, these pockets are well resolved, revealing a bound ATP that is contacted by canonical Walker A (K387), Walker B (E455), sensor-1 (N496), and sensor-2 (R620) residues (Figures 2E and S2I). The Arg-finger (R561) is provided by the neighboring clockwise protomer, and positioned one step lower along the substrate, contacting the γ-phosphate of ATP in protomers P3–P5 (Figures 2E and S2I). For protomer P2, ATP is present, but the Arg-finger from P1 is positioned further away and not in contact, indicating an intermediate state (Figure S2I). Notably, ATP-bound states are only found for substrate-engaged protomers (Figures 2A and S2I). Density for the nucleotide is more poorly resolved in protomers P1 and P6 at the spiral seam (Figures 2A and S2I). The nucleotide is absent from P6, indicating an apo state, whereas P1 is likely ADP bound. Thus, post-hydrolysis states coincide with substrate release at the seam. Thus, $_{PARL}$Skd3 may employ a conserved hydrolysis cycle similar to other AAA+ translocases (Gates et al., 2017; Puchades et al., 2017; Rizo et al., 2019). Based on this model, ATP hydrolysis and substrate release occur at the lower contact sites in the spiral (P1), whereas ATP binding promotes substrate re-binding to the top position (P5) along the substrate, enabling a rotary mechanism involving two residue steps along the substrate during processive translocation (Shorter and Southworth, 2019). However, other kinetic paths or non-processive events may also occur (Durie et al., 2019; Fei et al., 2020; Lin et al., 2022).

ANKs mediate $_{PARL}$Skd3 dodecamerization and enable disaggregase activity

The ANK is an unusual feature of Skd3 that is required for disaggregase activity (Cupo and Shorter, 2020b). Cryo-EM of SEC-purified $_{PARL}$Skd3^{NBD}, which lacks the ANK domain, reveals well-resolved single hexamers but no dodecamers (Figure S3A) (Wu et al., 2022). Thus, the ANK is not required for hexamerization, but is important for stabilizing the dodecamer. SEC indicates that the dodecamer predominates in the presence of substrate (Figures 1B and S1C). However, the dodecamer is less well represented following 2D and 3D cryo-EM analysis, with ~15% of particles possessing the three-ring architecture of class 2 (Figure S1F). Moreover, flexibility of the ANKs and the tilted arrangement of the AAA+ rings likely limit structure determination of the full dodecamer complex from class 2. Nonetheless, two full Skd3 hexamer models could be docked into the low-resolution class 2 map, revealing that the ANKs mediate contacts between the two hexamers (Figure S3B; Table S1). Resolution of the more poorly resolved NBD ring was insufficient to identify substrate in the channel, whereas density is present in the second NBD ring, which is likely casein contacted by pore loops from five protomers (Figure S3B). Conversely, in addition to the high-resolution AAA+ ring, the final map of the hexamer class (class 1) contains strong globular density extending from the N-terminal face that is likely the helical bundles of ankyrin repeats (Figure 1D). Thus, analysis of the full hexamer with the ANKs was further pursued with the class 1 map.

Structural information for the Skd3 ANK is unavailable. Thus, we used the Alpha-fold to model the ANK (Jumper et al., 2021). This secondary structural model is predicted with high confidence based on the pLDDT score and low predicted align error values (Figures S3C and S3D). Confidence was highest in the ANK and NBD domains (Figure S3D). Based on the Alpha-fold model, the ANK adopts four two-helix bundle structures that match canonical ANKs (Figure 3A). Starting at

Figure 3. The ANK mediates head-to-head contacts required for dodecamerization

(A) Schematic and model of $_{PARL}$Skd3 ANK, colored-based repeat number and linker.

(B) Side (left) and top (right) views of the filtered class 1 map and docked model, colored as in (A), identifying ANK position.

(C and D) Overlay of two different classes resolved from focus classification around P3 identifying rotation of the ANK region (arrow).

(E) SEC of $_{PARL}$Skd3 (black), $_{PARL}$Skd3$^{Δ1-2}$ (blue), $_{PARL}$Skd3^{ΔL} (green), and $_{PARL}$Skd3$^{Δ3-4}$ (red) incubated with ATPγS and casein. Vertical bars indicate molecular weight standards: thyroglobulin (669 kDa), ferritin (440 kDa), and ovalbumin (43 kDa), and are representative of $_{PARL}$Skd3 dodecamer (gray), hexamer (cyan), or monomer (magenta) size.

(F) ATPase activity of $_{PARL}$Skd3, $_{PARL}$Skd3$^{Δ1-2}$, $_{PARL}$Skd3^{ΔL}, $_{PARL}$Skd3$^{Δ3-4}$, and Hsp104. ATPase activity was compared with $_{PARL}$Skd3 using one-way ANOVA and a Dunnett's multiple comparisons test (n = 3–6, individual data points shown as dots, bars are mean ± SEM, ****p < 0.0001).

(G) Luciferase disaggregase activity of $_{PARL}$Skd3, $_{PARL}$Skd3$^{Δ1-2}$, $_{PARL}$Skd3^{ΔL}, $_{PARL}$Skd3$^{Δ3-4}$, and Hsp104 plus Hsp70 and Hsp40. Luciferase activity was normalized to Hsp104 plus Hsp70 and Hsp40. Disaggregase activity was compared with $_{PARL}$Skd3 using one-way ANOVA and a Dunnett's multiple comparisons test (n = 3, individual data points shown as dots, bars show mean ± SEM, ****p < 0.0001).

(H) 2D class averages of $_{PARL}$Skd3$^{Δ1-2}$ (top) and $_{PARL}$Skd3 (bottom) with the middle band of ANK density indicated (*). Note that the triple-hexamer arrangement (top right) is only found for $_{PARL}$Skd3$^{Δ1-2}$. Scale bar, 100 Å.

(I) Dodecamer map and model of $_{PARL}$Skd3$^{Δ1-2}$ colored by individual domains (left). Color-zoned map of substrate (yellow) present in the central channel of each AAA+ ring with $_{PARL}$Skd3$^{Δ1-2}$ model docked in (middle, right).

(J) Dodecamer map and model of $_{PARL}$Skd3$^{Δ1-2}$ showing ankyrin-repeat interactions across hexamers. See also Figure S3 and Video S2.

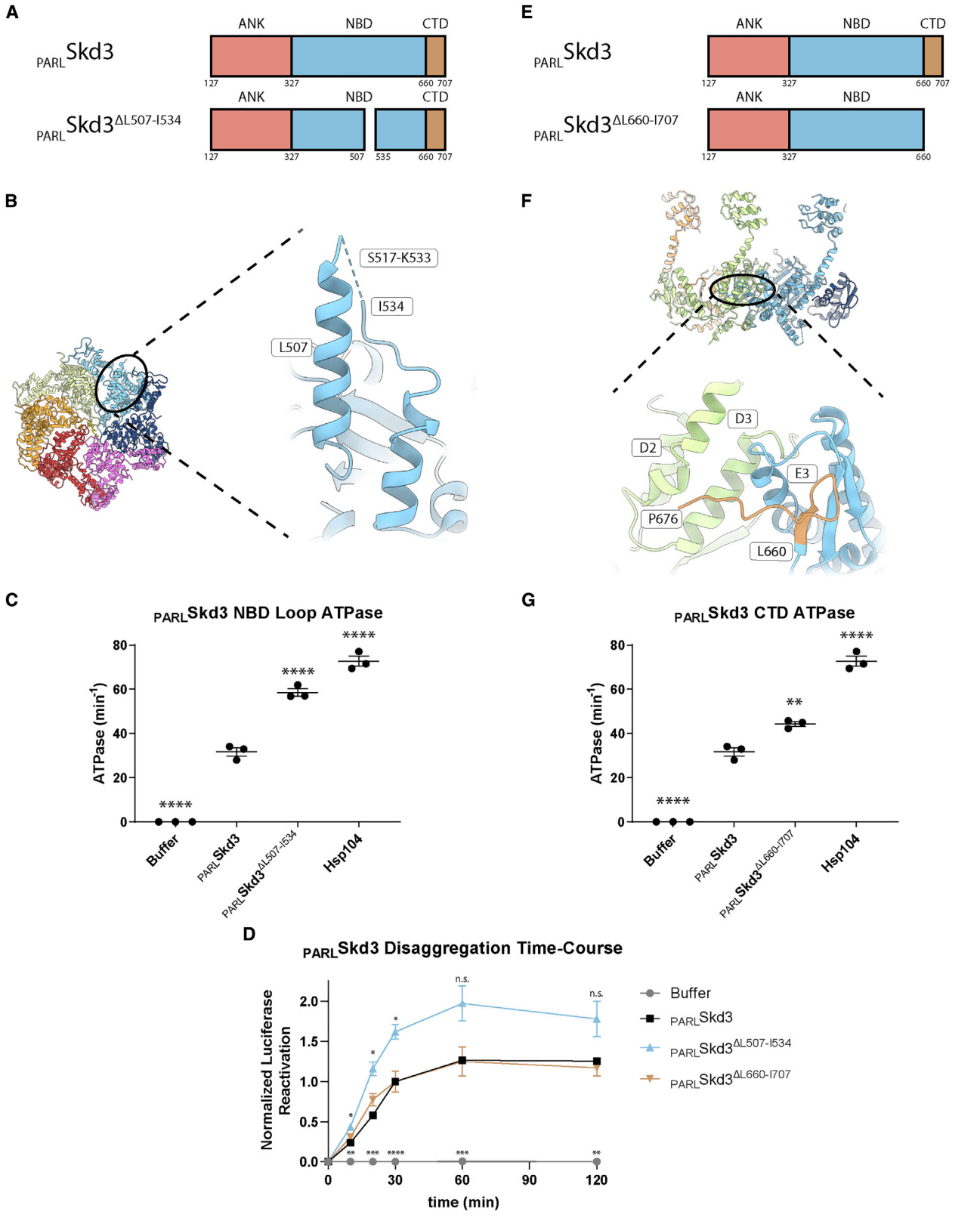

(legend on next page)

the N terminus, this structure consists of two ankyrin repeats (1 and 2), a 66-residue linker (L) that is mostly disordered, and two further ankyrin repeats (3 and 4) (Figure 3A). The linker is the exact length of two ankyrin repeats and has cryptic elements of ankyrin repeats within its primary sequence (Figure S3F). Alpha-fold predicts some helical regions within the linker, and these regions partially align to the other repeats (Figures 3A, S3C, and S3D). Thus, the linker may impart some ankyrin-like functions. Notably, repeat 4 forms an extended helix that transitions directly into the N-terminal region of the NBD without a separate linker between domains (Figure 3A). This continuous helix likely stabilizes the position of the ANKs given that interprotomer contacts are not present in the ANK ring. The four ankyrin repeats bundle together in the Alpha-fold model and dock well into the globular density adjacent to the NBD (Figure 3B; Video S1). The density for the ANK is more prominent for protomers P2–P5, which are bound to the substrate and better resolved compared with the spiral seam (Figure 3B). To further resolve the ANK, focus classification was performed on the P3 ANK. Resulting classes reveal that the ANK adopts different positions, indicating the flexibility of the ankyrin-repeat 4/NBD connecting helix (Figures 3C, 3D, and S3E). Notably, class 1 contains additional density that projects from the globular ANKs toward the central channel and is likely the linker (Figure S3E).

To assess how specific ANK regions enable Skd3 function, we generated $_{PARL}$Skd3 variants with ankyrin repeats 1 and 2 deleted (ΔY127-G196, $_{PARL}$Skd3$^{\Delta 1\text{-}2}$), the linker deleted (ΔD197-A262, $_{PARL}$Skd3$^{\Delta L}$), or ankyrin repeats 3 and 4 deleted (ΔS263-K325, $_{PARL}$Skd3$^{\Delta 3\text{-}4}$; Figure S3G). In the presence of casein and ATPγS, $_{PARL}$Skd3$^{\Delta 1\text{-}2}$ and $_{PARL}$Skd3$^{\Delta 3\text{-}4}$ formed predominantly dodecamers like $_{PARL}$Skd3 (Figures 1B and 3E). By contrast, $_{PARL}$Skd3$^{\Delta L}$ exhibited reduced dodecamer formation, and was shifted more toward hexamers (Figure 3E). Unlike $_{PARL}$Skd3^{NBD}, which exhibits reduced ATPase activity (Cupo and Shorter, 2020b), $_{PARL}$Skd3$^{\Delta 1\text{-}2}$, $_{PARL}$Skd3$^{\Delta L}$, and $_{PARL}$Skd3$^{\Delta 3\text{-}4}$ had similar ATPase activity to $_{PARL}$Skd3 (Figure 3F). Thus, a portion of the N-terminal ANK is required to maintain $_{PARL}$Skd3 ATPase activity. Nonetheless, $_{PARL}$Skd3$^{\Delta 1\text{-}2}$, $_{PARL}$Skd3$^{\Delta L}$, and $_{PARL}$Skd3$^{\Delta 3\text{-}4}$ exhibited reduced disaggregase activity (Figure 3G), indicating that the ANK enables $_{PARL}$Skd3 to efficiently couple ATP hydrolysis to protein disaggregation. Deletion of the linker had the largest effect (Figure 3G). $_{PARL}$Skd3$^{\Delta L}$ is impaired in dodecamer formation (Figure 3E). Thus, dodecamerization may promote disaggregase activity. We suggest that the ANKs play multiple roles in protein disaggregation, including dodecamerization, potentially supported by the linker, and substrate engagement mediated by ankyrin repeats 1–4 (Wu et al., 2022).

EM indicated that $_{PARL}$Skd3$^{\Delta 1\text{-}2}$ forms more stable dodecamers than $_{PARL}$Skd3$^{\Delta L}$ and $_{PARL}$Skd3$^{\Delta 3\text{-}4}$. Thus, we investigated $_{PARL}$Skd3$^{\Delta 1\text{-}2}$ further by cryo-EM. 2D averages of $_{PARL}$Skd3$^{\Delta 1\text{-}2}$ show a well-resolved middle ring of ANKs that is smaller in diameter than $_{PARL}$Skd3 (Figure 3H). 3D classification of $_{PARL}$Skd3$^{\Delta 1\text{-}2}$ identified three distinct forms. Class 1 and class 2 are dodecamers with different relative positions of the AAA+ rings, whereas class 3 is a trimer of hexamers (Figures S3H and S3I). Refinement of class 1 was pursued due to the more homogeneous arrangement of the ANK ring and improved density for the second AAA+ ring compared with the $_{PARL}$Skd3 complex (Figures 3I, 3J, and S3J–S3M). Notably, we identify density in the two AAA+ channels that corresponds to the substrate, indicating that both AAA+ rings can bind substrate in the dodecamer (Figure 3I), Although the resolution was low (~9 Å), a dodecameric model with ankyrin repeats 3 and 4 fit well into the density, and revealed head-to-head ANK contacts around the central ring that mediate dodecamer formation (Figures 3I and 3J; Table S1; Video S2). Given that $_{PARL}$Skd3$^{\Delta 3\text{-}4}$ can also form dodecamers, as can $_{PARL}$Skd3$^{\Delta L}$ to a lesser extent (Figure 3E), our findings indicate plasticity in how the ANK mediates cross-contacts to form dodecamers. We suggest that deleting specific ankyrin repeats or the linker reduces this interactive plasticity and disaggregase activity (Figure 3G).

A unique insertion within the $_{PARL}$Skd3 NBD regulates the AAA+ motor

Skd3 contains an insertion (residues L507-I534) within the NBD that is conserved across Skd3 homologs but is not found in Hsp104 or other HCLR class AAA+ proteins (Figures 4A and S4A) (Cupo and Shorter, 2020b). We modeled part of the insertion, but 17 residues (517–533) were missing (Figures 4B and S4B). The insertion extends past the loop that is found in Hsp104 (Figure S4C) and protrudes from the hexamer exterior (Figure 4B). Purified $_{PARL}$Skd3$^{\Delta L507\text{-}I534}$ formed large oligomers that are not observed for $_{PARL}$Skd3 (Figure S4D). However, upon addition of casein, $_{PARL}$Skd3$^{\Delta L507\text{-}I534}$ forms primarily dodecamers (Figure S4D). $_{PARL}$Skd3$^{\Delta L507\text{-}I534}$ had elevated ATPase and disaggregase activity compared with $_{PARL}$Skd3 (Figures 4C and 4D). Thus, the L507-I534 insertion is a regulatory element, which slows $_{PARL}$Skd3 ATPase activity and tunes disaggregase activity. The location of the L507-I534 insertion on the

Figure 4. An NBD insertion and the CTD regulate $_{PARL}$Skd3

(A) Domain architecture of $_{PARL}$Skd3 and $_{PARL}$Skd3$^{\Delta L507\text{-}I534}$.

(B) Top view of $_{PARL}$Skd3 hexamer and expanded view of NBD-insertion region residues 449–552 (residues 517–533 are not resolved [dashed line]) in P4.

(C) ATPase activity of $_{PARL}$Skd3, $_{PARL}$Skd3$^{\Delta L507\text{-}I534}$, and Hsp104. Data are from the same experiments as Figure 3F. ATPase activity was compared with $_{PARL}$Skd3 using one-way ANOVA and a Dunnett's multiple comparisons test (n= 3, individual data points shown as dots, bars are mean ± SEM, ****p < 0.0001).

(D) Luciferase disaggregation kinetics showing that $_{PARL}$Skd3$^{\Delta L507\text{-}I534}$ has enhanced disaggregase activity at early times, whereas $_{PARL}$Skd3$^{\Delta L660\text{-}I707}$ does not. Luciferase activity was normalized to the $_{PARL}$Skd3 30 min time point. Luciferase activity was compared with $_{PARL}$Skd3 using one-way ANOVA and a Dunnett's multiple comparisons test (n = 3, values are means ± SEM, *p < 0.05, **p < 0.01, ***p < 0.001, ****p < 0.0001).

(E) Domain architecture of $_{PARL}$Skd3 and $_{PARL}$Skd3$^{\Delta L660\text{-}I707}$.

(F) Side view of $_{PARL}$Skd3 hexamer and expanded view of P3–P4 with the P4 CTD model (brown) shown adjacent to P3 with potential interacting helices indicated.

(G) ATPase activity of $_{PARL}$Skd3 and $_{PARL}$Skd3$^{\Delta L660\text{-}I707}$. Data are from the same experiments as Figure 3F. ATPase activity was compared with $_{PARL}$Skd3 using one-way ANOVA and a Dunnett's multiple comparisons test (n = 3, individual data points shown as dots, bars show mean ± SEM, **p < 0.01, ****p < 0.0001). See also Figure S4.

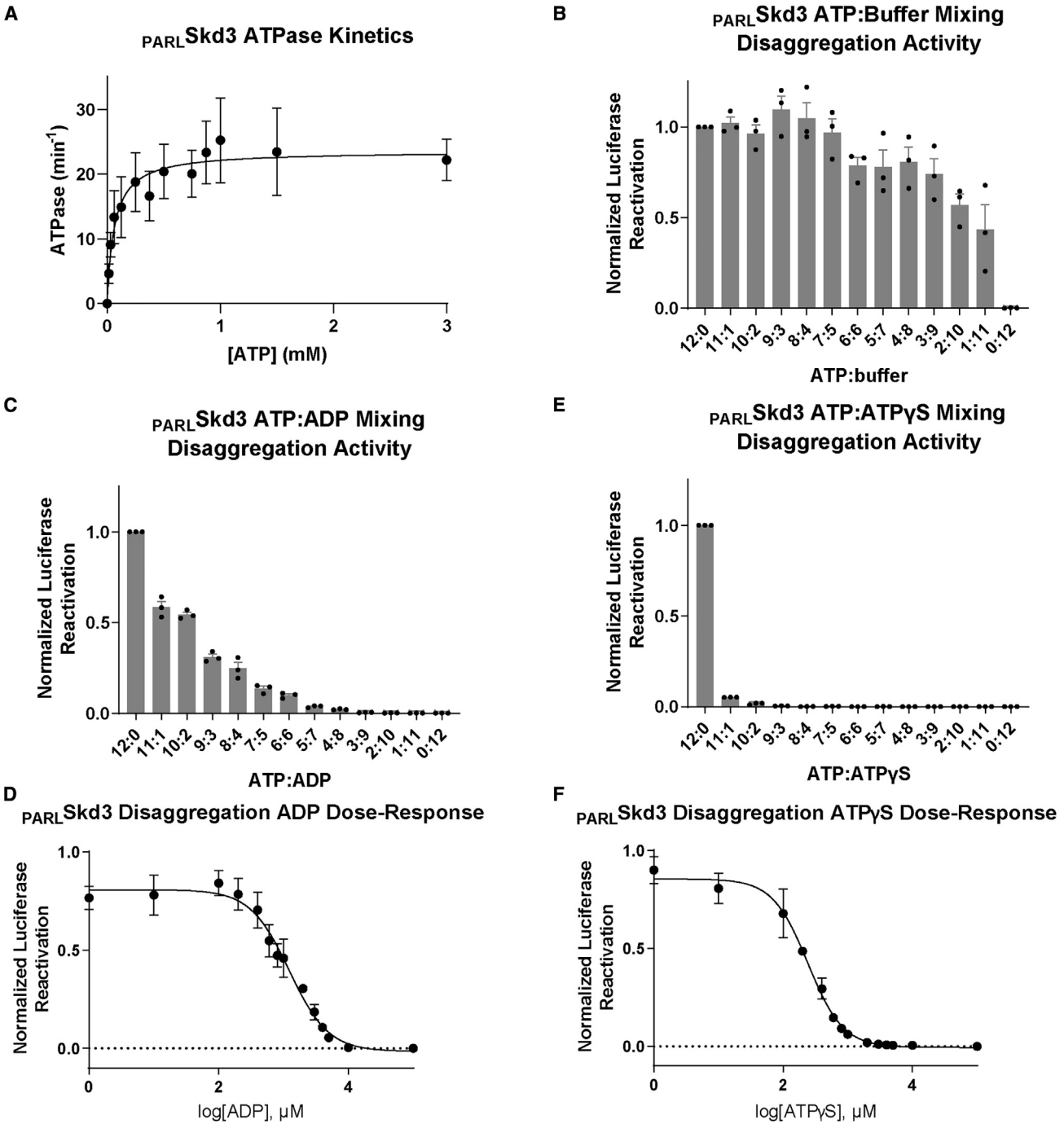

Figure 5. $_{PARL}$Skd3 is functional at low ATP concentrations

(A) Michaelis-Menten plot of $_{PARL}$Skd3 ATPase activity. $V_{max} \sim 23.6$ min^{-1} and $K_M \sim 64.6$ μM (n = 3, values are means ± SEM).

(B) Luciferase disaggregase activity of $_{PARL}$Skd3 at various ATP:buffer ratios. ATP concentrations used were 12:0 (5 mM), 11:1 (4.58 mM), 10:2 (4.17 mM), 9:3 (3.75 mM), 8:4 (3.33 mM), 7:5 (2.92 mM), 6:6 (2.5 mM), 5:7 (2.08 mM), 4:8 (1.67 mM), 3:9 (1.25 mM), 2:10 (0.83 mM), 1:11 (0.42 mM), and 0:12 (0 mM). Disaggregase activity was normalized to $_{PARL}$Skd3 plus ATP (n = 3, individual data points shown as dots, bars show mean ± SEM).

(C) Luciferase disaggregase activity of $_{PARL}$Skd3 at various ATP:ADP ratios where the total nucleotide concentration was 5 mM. Disaggregase activity was normalized to $_{PARL}$Skd3 plus ATP (n= 3, individual data points shown as dots, bars show mean ± SEM).

(D) Luciferase disaggregase activity of $_{PARL}$Skd3 at a constant concentration of ATP (5 mM) and increasing ADP concentrations. Disaggregase activity was normalized to $_{PARL}$Skd3 plus ATP (n = 3, values are means ± SEM).

(legend continued on next page)

hexamer exterior could provide a site for regulatory factors to bind or post-translationally modify Skd3.

Deletion of the $_{PARL}$Skd3 CTD mildly stimulates ATPase activity

Deletion of the extended, acidic CTD of *S. cerevisiae* Hsp104 results in hexamerization defects (Mackay et al., 2008). Like Hsp104 and in contrast to other HCLR clade AAA+ proteins, Skd3 has an extended CTD from residues 660 to 707 (Figure 4E) (Cupo and Shorter, 2020b). However, the Skd3 CTD is patterned with acidic and basic residues, whereas the Hsp104 CTD is acidic (Cupo and Shorter, 2020b). In the $_{PARL}$Skd3 reconstruction, 14 residues of the CTD were evident in protomers P3–P5 (Figure 1D). These CTD residues fit along the side of the adjacent protomer and are near helices D2 and D3 (Figures 4F and S2F). Residues within ~4 Å of the CTD include E340 and Q341 in D2, and R362 in D3. Additional contacts may occur with helix E3 of the same protomer (Figures 4F and S2F). We purified $_{PARL}$Skd3 lacking the CTD ($_{PARL}$Skd3$^{\Delta L660\text{-}I707}$), which formed hexamers and dodecamers similar to $_{PARL}$Skd3 (Figures 1A and S4E). $_{PARL}$Skd3$^{\Delta L660\text{-}I707}$ exhibited mildly increased ATPase activity (Figure 4G), whereas disaggregase activity was similar to $_{PARL}$Skd3 (Figure 4D). Thus, the CTD enables efficient coupling of $_{PARL}$Skd3 ATPase and disaggregase activity. We suggest that the $_{PARL}$Skd3 CTD plays a different role than the Hsp104 CTD.

$_{PARL}$Skd3 is functional at low ATP concentrations

Mitochondria maintain lower ratios of ATP:ADP and lower ATP concentrations than the cytoplasm (Gellerich et al., 2002; Heldt et al., 1972; Imamura et al., 2009). To determine how $_{PARL}$Skd3 might operate under various nucleotide conditions, we established that $_{PARL}$Skd3 ATPase activity has a V_{max} of ~24 min^{-1} and a K_M of ~65 μM (Figure 5A). By contrast, the K_M of Hsp104 is ~5–11 mM (Grimminger et al., 2004; Schirmer et al., 1998). $_{PARL}$Skd3 maintains disaggregase activity at low ATP concentrations, including ~50% disaggregase activity at the lowest ATP concentration tested (0.434 mM) (Figure 5B). Thus, $_{PARL}$Skd3 is likely adapted to operate effectively at lower ATP concentrations than Hsp104.

$_{PARL}$Skd3 disaggregase activity is inhibited by ADP

Hsp104 is sharply inhibited by mixing ADP with ATP (Grimminger et al., 2004; Hattendorf and Lindquist, 2002; Klosowska et al., 2016). Even a 5:1 ATP:ADP ratio diminishes Hsp104 activity (Klosowska et al., 2016). To test the effect of ADP on $_{PARL}$Skd3, we assessed $_{PARL}$Skd3 disaggregase activity under different ATP:ADP ratios while keeping the total nucleotide concentration constant. $_{PARL}$Skd3 is inhibited by ADP, but maintains ~50% activity at a 5:1 ATP:ADP ratio (Figure 5C), which inactivates Hsp104 (Klosowska et al., 2016). The half-maximal inhibitory concentration (IC_{50}) of ADP at a constant concentration of ATP (5 mM) was ~1.2 mM (Figure 5D). Thus, $_{PARL}$Skd3 is less sensitive than Hsp104 to inhibition by ADP and is likely adapted to function at the lower ATP:ADP ratios found in mitochondria.

$_{PARL}$Skd3 disaggregase activity is sharply inhibited by ATPγS

Next, we assessed how $_{PARL}$Skd3 disaggregase activity is affected by the slowly hydrolyzable ATP analog, ATPγS. Like Hsp104, $_{PARL}$Skd3 is inactive in the presence of ATPγS as the sole nucleotide (Cupo and Shorter, 2020b; DeSantis et al., 2012). However, Hsp104 disaggregase activity against disordered aggregates can be stimulated at specific ratios of ATP:ATPγS (~3:1–1:5), whereas Hsp104 disaggregase activity against amyloid is inhibited by ATPγS in the presence of ATP (DeSantis et al., 2012). Thus, Hsp104 employs distinct mechanisms of subunit collaboration to disaggregate disordered aggregates versus amyloid (DeSantis et al., 2012). To assess the effect of ATPγS on $_{PARL}$Skd3, we measured $_{PARL}$Skd3 disaggregase activity under different ATP:ATPγS ratios while keeping the total nucleotide concentration constant. $_{PARL}$Skd3 is sharply inhibited by ATPγS (Figure 5E). Even an 11:1 ATP:ATPγS ratio inhibits $_{PARL}$Skd3 (Figure 5E). The IC_{50} of ATPγS at a constant concentration of ATP (5 mM) was ~242 μM (Figure 5F). Thus, in contrast to Hsp104 (DeSantis et al., 2012), $_{PARL}$Skd3 disaggregase activity against disordered aggregates is not stimulated by ATP:ATPγS mixtures. The distinctive responses of $_{PARL}$Skd3 to ADP and ATPγS reveal differences in how $_{PARL}$Skd3 and Hsp104 disaggregase activity are regulated. The sharp inhibition of $_{PARL}$Skd3 disaggregase activity by ATPγS indicates that $_{PARL}$Skd3 is sensitive to individual subunits that hydrolyze ATP slowly.

$_{PARL}$Skd3 is a subglobally cooperative protein disaggregase

Next, to define mechanochemical coupling mechanisms of $_{PARL}$Skd3, we used a mutant subunit doping strategy to assess how individual $_{PARL}$Skd3 subunits contribute to ATPase and disaggregase activity. We modeled Skd3 as a hexamer, which forms the functional AAA+ cassette (Figure 2E). In this strategy, mutant $_{PARL}$Skd3 subunits defective in ATP hydrolysis or substrate binding are mixed with WT $_{PARL}$Skd3 subunits to generate heterohexameric ensembles according to a binomial distribution dictated by the WT:mutant ratio (Figure 6A). As mutant $_{PARL}$Skd3 concentration in the mixture increases, the probability of mutant $_{PARL}$Skd3 incorporation into a $_{PARL}$Skd3 hexamer increases (Figure 6A). This approach has revealed mechanochemical coupling mechanisms of other NTPases, including Hsp104/ClpB (DeSantis et al., 2012; Moreau et al., 2007; Shivhare et al., 2019; Werbeck et al., 2008).

This strategy depends on robust formation of randomized heterohexamer ensembles, which requires exchange of subunits between WT and mutant $_{PARL}$Skd3 hexamers such that mutant

(E) Luciferase disaggregase activity of $_{PARL}$Skd3 at various ATP:ATPγS ratios where the total nucleotide concentration was 5 mM. Disaggregase activity was normalized to $_{PARL}$Skd3 plus ATP (n = 3, individual data points shown as dots, bars show mean ± SEM).
(F) Luciferase disaggregase activity of $_{PARL}$Skd3 at a constant concentration of ATP (5 mM) and increasing ATPγS concentrations. Disaggregase activity was normalized to $_{PARL}$Skd3 plus ATP (n = 3, data shown as mean ± SEM).

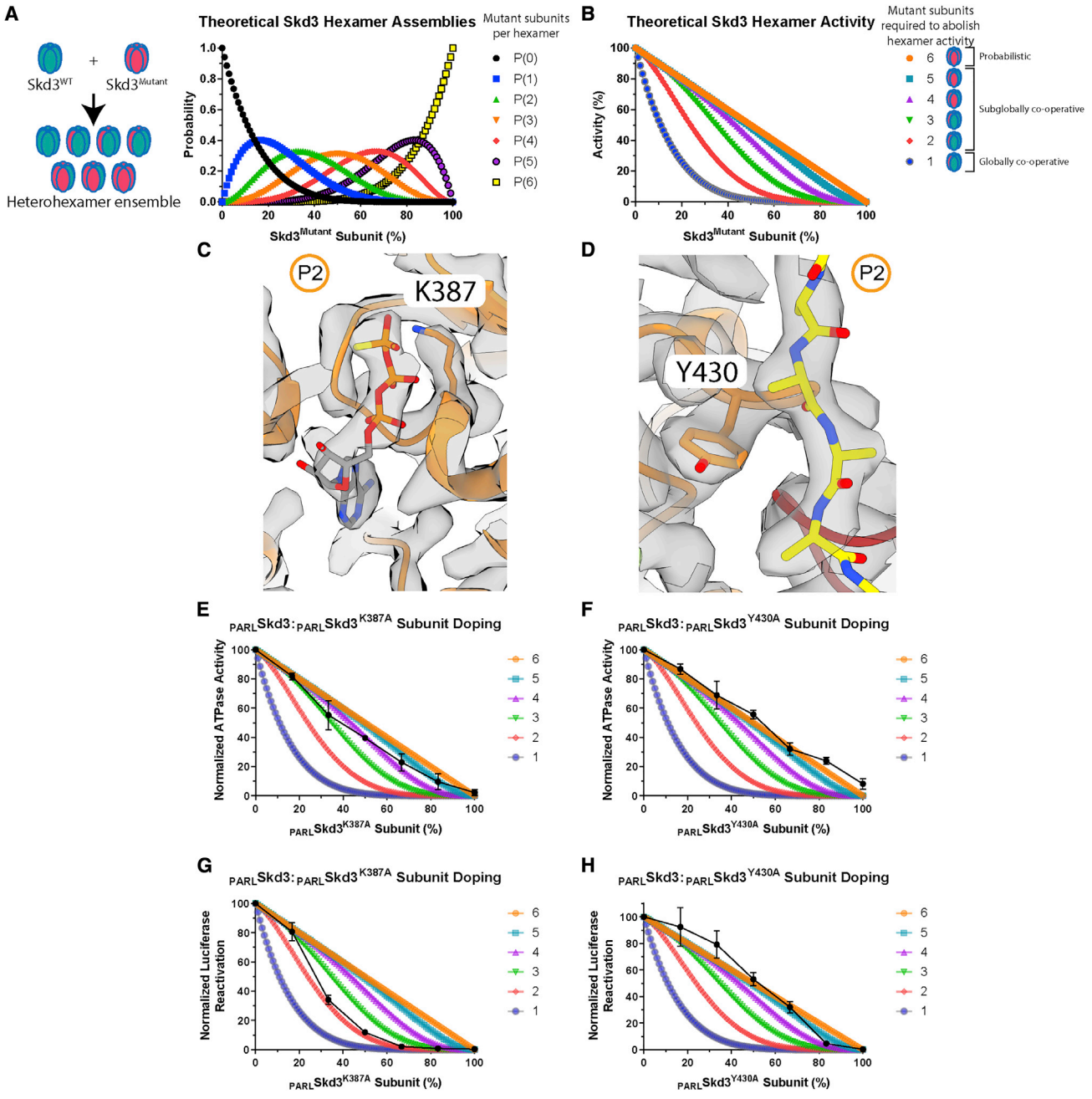

Figure 6. Skd3 is a subglobally cooperative disaggregase

(A) Theoretical $_{PARL}$Skd3 hexamer ensembles containing zero (black), one (blue), two (green), three (orange), four (red), five (purple), and six (yellow) mutant subunits as a function of the fraction of mutant subunit.

(B) Theoretical $_{PARL}$Skd3 activity curves where one or more (blue), two or more (red), three or more (green), four or more (purple), five or more (light blue), or six (orange) mutant subunits ablate hexamer activity. In a probabilistic model, six mutant subunits per hexamer ablate activity. In a subglobally cooperative model, two to five mutant subunits per hexamer ablate activity. In a globally cooperative model, one mutant subunit per hexamer ablates activity.

(C and D) Protomer P2 with nucleotide and K387 shown in (C) or substrate and Y430 shown in (D).

(E and F) ATPase activity of $_{PARL}$Skd3 mixed with various ratios of $_{PARL}$Skd3^{K387A} (E) or $_{PARL}$Skd3^{Y430A} (F). ATPase activity was normalized to $_{PARL}$Skd3 (n = 3, black dots are means ± SEM).

(G and H) Luciferase disaggregase activity of $_{PARL}$Skd3 mixed with various ratios of $_{PARL}$Skd3^{K387A} (G) or $_{PARL}$Skd3^{Y430A} (H). Disaggregase activity was normalized to $_{PARL}$Skd3 (n = 3, black dots are means ± SEM). See also Figure S5.

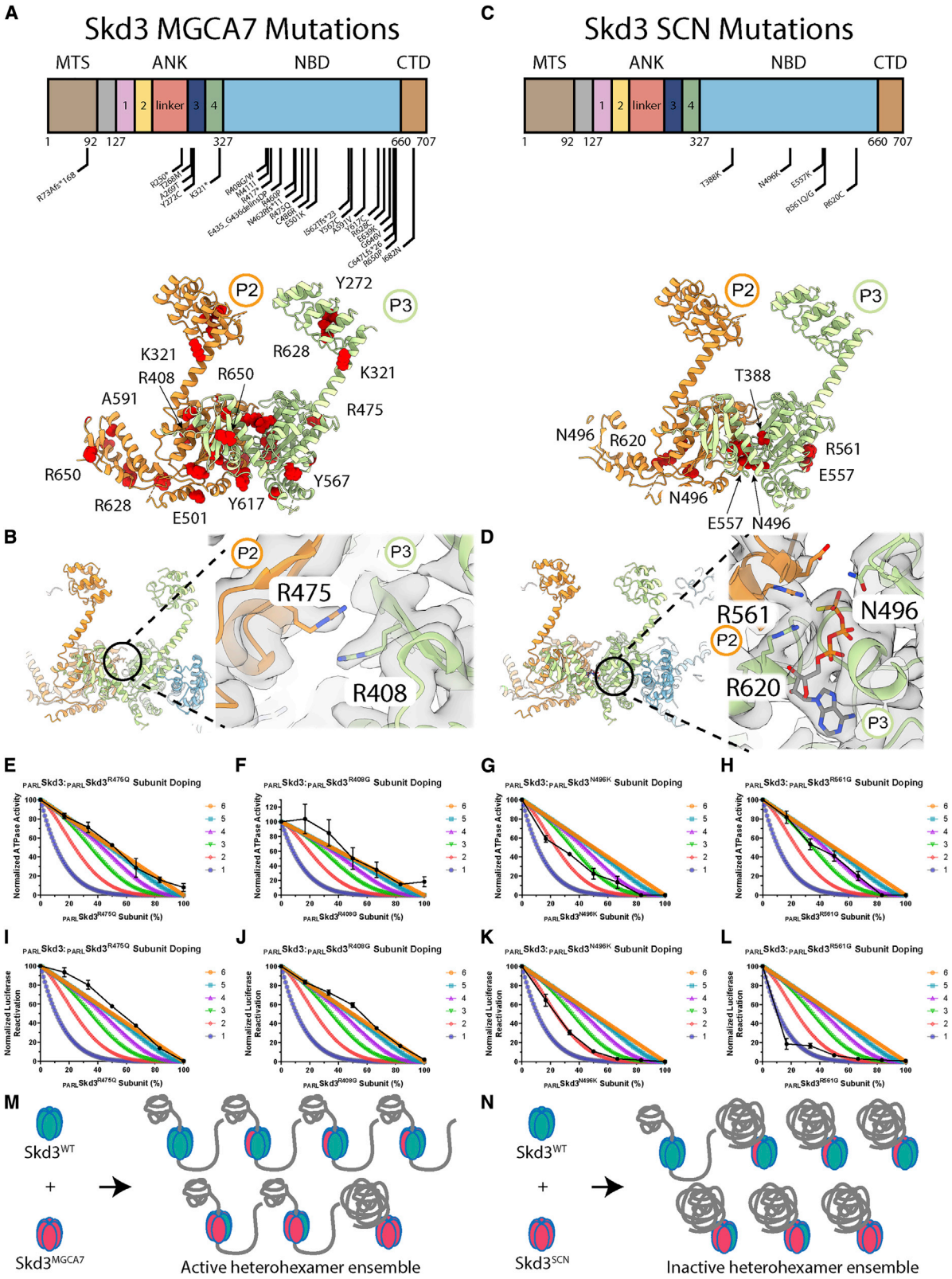

(legend on next page)

subunits mix equally well into heterohexamers as WT (Figure 6A). To assess subunit mixing, we labeled $_{PARL}$Skd3 with Alexa 488 or Alexa 594, which can form a Förster resonance energy transfer (FRET) pair. Labeled $_{PARL}$Skd3 retained ATPase and disaggregase activity (Figures S5A and S5B). We mixed Alexa 488-labeled $_{PARL}$Skd3 and Alexa 594-labeled $_{PARL}$Skd3 in the absence of substrate, where the hexamer is more populated (Figures S1B and S1C). Hence, FRET likely reflects subunit mixing within the hexamer. For WT $_{PARL}$Skd3, a robust FRET signal was observed within a few minutes, indicating subunit mixing on the minute timescale similar to Hsp104 (Figure S5D) (DeSantis et al., 2012). Thus, $_{PARL}$Skd3 forms dynamic hexamers that exchange subunits on the minute timescale.

Importantly, mutant $_{PARL}$Skd3 subunits were effectively incorporated into WT $_{PARL}$Skd3 hexamers (Figure S5D). $_{PARL}$Skd3^{K387A} (Walker A) subunits likely incorporate into WT $_{PARL}$Skd3 hexamers as effectively as WT $_{PARL}$Skd3 subunits, whereas $_{PARL}$Skd3^{Y430A} (pore loop) subunits incorporated into WT $_{PARL}$Skd3 hexamers ~16% less effectively than WT $_{PARL}$Skd3 subunits (Figure S5D). Thus, specific mutant $_{PARL}$Skd3 subunits incorporate effectively into WT $_{PARL}$Skd3 hexamers, indicating that the $_{PARL}$Skd3 mechanism can be probed via mutant doping studies.

This rapid subunit exchange enables formation of $_{PARL}$Skd3 heterohexamer ensembles comprised of WT and mutant subunits according to a binomial distribution (Figure 6A). Using this distribution, we can predict how $_{PARL}$Skd3 activity would be inhibited at various WT:mutant ratios if a specific number of $_{PARL}$Skd3 mutant subunits inactivate the hexamer (Figure 6B). For example, if all six $_{PARL}$Skd3 subunits must work together, then one mutant subunit would abolish hexamer activity (Figure 6B, dark blue curve). By contrast, if the activity of a single $_{PARL}$Skd3 subunit within the hexamer is sufficient, then some activity would still be observed with five mutant subunits per hexamer, and only six mutant subunits would abolish activity (Figure 6B, orange line). By comparing experimental data with theoretical plots, we can determine whether subunit collaboration within $_{PARL}$Skd3 hexamers is probabilistic (six mutant subunits abolish activity), subglobally cooperative (two to five mutant subunits abolish activity), or globally cooperative (one mutant subunit abolishes activity).

We titrated $_{PARL}$Skd3 with buffer over the concentration range of the subunit doping ATPase assay and found a linear decline in ATPase activity (Figure S5E). Thus, when titrating mutant $_{PARL}$Skd3, a sharper than linear decline in ATPase activity indicates inhibitory effects of mutant subunits incorporated into hexamers. We also titrated $_{PARL}$Skd3 with buffer over a range of concentrations to assess disaggregase activity (Figure S5F). We selected saturating $_{PARL}$Skd3 concentrations to ensure that any observed effects on disaggregase activity upon mixing WT and mutant are not caused by a mere decrease in the concentration of WT $_{PARL}$Skd3 (DeSantis et al., 2012; Werbeck et al., 2008).

$_{PARL}$Skd3^{K387A} (Walker A) and $_{PARL}$Skd3^{Y430A} (pore loop) are inactive for ATPase and disaggregase activity (Cupo and Shorter, 2020b). The Walker A residue, K387, contacts the β- and γ-phosphate of ATP and a K387A mutation is predicted to reduce ATP binding and hydrolysis (Figure 6C) (Puchades et al., 2020). The pore-loop tyrosine, Y430, engages substrate, and a Y430A mutation is predicted to reduce substrate binding (Figures 2B and 6D) (Cupo and Shorter, 2020b). We assembled heterohexamer ensembles of $_{PARL}$Skd3 with $_{PARL}$Skd3^{K387A} (Walker A) or $_{PARL}$Skd3^{Y430A} (pore loop). $_{PARL}$Skd3^{K387A} (Walker A) subunits inhibited $_{PARL}$Skd3 ATPase activity in a manner that suggested the incorporation of approximately three to five mutant subunits inactivates the hexamer (Figure 6E). Thus, basal Skd3 ATPase activity appears to be subglobally cooperative. By contrast, titrating $_{PARL}$Skd3^{Y430A} (pore loop) subunits did not affect $_{PARL}$Skd3 ATPase activity any more than dilution in buffer (Figure 6F). Hence, the ATPase activity of the $_{PARL}$Skd3 hexamer is more resistant to pore-loop mutant subunits than Walker A mutant subunits. Our findings contrast with observations made with Hsp104 (DeSantis et al., 2012), where Walker A mutant subunits do not affect the ATPase activity of the hexamer more than dilution in buffer, and pore-loop mutant subunits have no effect (DeSantis et al., 2012). Thus, Hsp104 and $_{PARL}$Skd3 display distinct subunit cooperativity with respect to ATP hydrolysis.

We next examined how $_{PARL}$Skd3^{K387A} (Walker A) and $_{PARL}$Skd3^{Y430A} (pore loop) subunits affected $_{PARL}$Skd3 disaggregase activity. Incorporation of two $_{PARL}$Skd3^{K387A} (Walker A) subunits is sufficient to inactivate the $_{PARL}$Skd3 hexamer (Figure 6G). Thus, $_{PARL}$Skd3 hexamers are sensitive to individual subunits that are unable to bind or hydrolyze ATP due to a defective Walker A motif. This finding reinforces our previous observation that $_{PARL}$Skd3 disaggregase activity is sharply inhibited by the slowly hydrolyzable ATP analog, ATPγS (Figures 5E and 5F). By contrast, five $_{PARL}$Skd3^{Y430A} (pore loop) subunits are needed to inactivate the $_{PARL}$Skd3 hexamer (Figure 6H). Even though $_{PARL}$Skd3^{Y430A} has reduced ATPase activity (Cupo and Shorter, 2020b), this ATPase defect is more readily buffered by WT

Figure 7. SCN-linked subunits inhibit $_{PARL}$Skd3 activity more severely than MGCA7-linked $_{PARL}$Skd3 subunits

(A) Location of MGCA7-linked biallelic mutations in Skd3 (top). Model of protomers P2 and P3 with MGCA7-linked mutations colored in red (bottom).

(B) Model of back protomers colored by individual protomers (left). Interaction interface of residue R475 from protomer P2 and residue R408 from protomer P3.

(C) Location of SCN-linked mutations in Skd3 (top). Model of protomers P2 and P3 with SCN-linked mutations colored in red.

(D) Model of back protomers colored by individual protomers (left). Interaction interface of residues E557 and R561 of protomer P2 and residues N496 and R620 from protomer P3 within the nucleotide-binding pocket of protomer P3.

(E–H) ATPase activity of $_{PARL}$Skd3 mixed with various ratios of $_{PARL}$Skd3^{R475Q} (E), $_{PARL}$Skd3^{R408G} (F), $_{PARL}$Skd3^{N496K} (G), or $_{PARL}$Skd3^{R561G} (H). ATPase activity was normalized to $_{PARL}$Skd3 (n = 3, black dots are means ± SEM).

(I–L) Luciferase disaggregase activity of $_{PARL}$Skd3 mixed with various ratios of $_{PARL}$Skd3^{R475Q} (I), $_{PARL}$Skd3^{R408G} (J), $_{PARL}$Skd3^{N496K} (K), or $_{PARL}$Skd3^{R561G} (L). Disaggregase activity was normalized to $_{PARL}$Skd3 (n = 3, black dots are means ± SEM).

(M) $_{PARL}$Skd3 hexamers containing a mixture of WT and MGCA7-linked subunits are typically active disaggregases.

(N) $_{PARL}$Skd3 hexamers containing a mixture of WT and SCN-linked subunits are typically less active disaggregases. See also Figure S6.

subunits upon incorporation into $_{PARL}$Skd3 hexamers (Figure 6F). Thus, insufficient substrate binding by the pore loops must contribute to inhibition by $_{PARL}$Skd3^{Y430A} subunits. We suggest that $_{PARL}$Skd3 utilizes a subglobally cooperative mechanism to disaggregate disordered luciferase aggregates. Specifically, at least five subunits must have a functional Walker A motif to bind and hydrolyze ATP and at least two subunits must be able to engage substrate tightly via Y430 for productive luciferase disaggregase activity. Our findings illustrate that $_{PARL}$Skd3 hexamers display robustness and can buffer a defined number of specific mutant subunits. For example, $_{PARL}$Skd3 hexamers can tolerate one subunit with a defective Walker A motif, and four subunits with a defective pore loop, and still drive luciferase disaggregation. This variable robustness has implications for SCN and MGCA7 etiology.

SCN-linked subunits inhibit $_{PARL}$Skd3 activity more severely than MGCA7-linked $_{PARL}$Skd3 subunits

We surveyed the location of disease-linked mutations in the Skd3 structure. Biallelic MGCA7-linked mutations are dispersed throughout Skd3 (Figure 7A) (Wortmann et al., 2015). MGCA7-linked mutations are found in the MTS, ANK, NBD, and CTD (Figure 7A). T268M, A269T, and Y272C cluster in ankyrin repeat 3 and are conserved residues of the ankyrin-repeat motif (Figure 7A). Specifically, residues T268 and A269 lie near the N-terminal portion of the first α helix in ankyrin repeat 3 (Figure S3F). Mutations at T268 and A269 might destabilize the α helix and disrupt ankyrin repeat 3 (Mosavi et al., 2002). MGCA7-linked mutations are also found in the large (e.g., M411I, R460P, C486R, and E501K) and small (e.g., A591V, R628C, and R650P) NBD subdomains (Figure 7A). Some MGCA7-linked NBD mutations, such as R475Q and R408G, are in residues that make interprotomer contacts (Figure 7B).

By contrast, SCN-linked mutations are found exclusively in the NBD and cluster within the nucleotide-binding pocket (Figures 7C and 7D) (Warren et al., 2022). Most of the SCN-linked mutations are in canonical AAA+ motifs. N496K mutates the sensor-1 motif, which coordinates the attacking water molecule relative to the γ-phosphate of ATP (Figures 2E, S2I, and 7D) (Puchades et al., 2020). R561G mutates the Arg finger, which contacts the γ-phosphate of ATP in the nucleotide-binding pocket of the adjacent protomer and is key for ATP hydrolysis (Figures 2E, S2I, and 7D) (Puchades et al., 2020). R620C mutates the sensor-2 motif, which contacts the β- and γ-phosphates of ATP (Figures 2E, S2I, and 7D) (Puchades et al., 2020). T388K is directly adjacent to the Walker A motif, is highly conserved among other HCLR clade AAA+ proteins, and faces into the nucleotide-binding pocket (Figures 2E and 7C). Finally, E557K lies within a conserved stretch of residues near the Arg finger and contacts the nucleotide (Figures 7C and 7D).

MGCA7-linked mutations impair disaggregase activity in a way that predicts disease severity (Cupo and Shorter, 2020b). However, MGCA7-linked mutations do not always impair ATPase activity (Cupo and Shorter, 2020b). By contrast, SCN-linked mutations invariably impair ATPase and disaggregase activity (Warren et al., 2022). It is not understood why SCN-linked mutations are dominant negative, whereas MGCA7-linked mutations are recessive. To assess how severely MGCA7-linked and SCN-linked variants affect WT $_{PARL}$Skd3 activity, we selected three MGCA-7 linked variants (R408G, R475Q, and A591V) and three SCN-linked variants (N496K, R561G, and R620C) for subunit doping studies (Figures 7A–7D) (Pronicka et al., 2017; Warren et al., 2022). All of these mutations severely impair disaggregase activity (Cupo and Shorter, 2020b; Warren et al., 2022). Likewise, these disease-linked variants have diminished ATPase activity, with the exception of the MGCA7-linked variant $_{PARL}$Skd3^{R408G}, which retains ~20% ATPase activity (Cupo and Shorter, 2020b; Warren et al., 2022).

We assessed the ability of the disease-linked $_{PARL}$Skd3 variants to form hexamers and dodecamers in the presence of ATPγS and absence of substrate. Unlike $_{PARL}$Skd3, which was shifted toward the hexameric form, two of the MGCA7-linked variants, $_{PARL}$Skd3^{R408G} and $_{PARL}$Skd3^{R475Q}, were shifted toward dodecamers (Figure S6A). By contrast, MGCA7-linked $_{PARL}$Skd3^{A591V} was shifted to lower-molecular-weight oligomers (Figure S6A). $_{PARL}$Skd3^{A591V} formed some hexamers, but dodecamers were reduced (Figure S6A). The SCN-linked variant, $_{PARL}$Skd3^{N496K}, was shifted toward hexamers like $_{PARL}$Skd3 (Figure S6B). The remaining SCN-linked variants, $_{PARL}$Skd3^{R561G} and $_{PARL}$Skd3^{R620C}, were shifted toward dodecamers (Figure S6B).

To test how severely disease-linked variants affected WT $_{PARL}$Skd3 activity, we mixed each disease-linked variant and WT $_{PARL}$Skd3 and assessed ATPase activity. FRET studies showed that disease-linked $_{PARL}$Skd3 subunits were effectively incorporated into WT $_{PARL}$Skd3 hexamers (Figures S6C and S6D). Addition of the MGCA7-linked variant $_{PARL}$Skd3^{R475Q} to $_{PARL}$Skd3 revealed that six $_{PARL}$Skd3^{R475Q} subunits are required to reduce ATPase activity to the same level as $_{PARL}$Skd3^{R475Q} (Figure 7E). $_{PARL}$Skd3^{R408G} retains ~20% of WT ATPase activity and five $_{PARL}$Skd3^{R408G} subunits per hexamer reduced ATPase activity to this level (Figure 7F). Likewise, five $_{PARL}$Skd3^{A591V} subunits per hexamer are required to eliminate ATPase activity (Figure S6E). Thus, MGCA7-linked subunits have mild inhibitory effects on the ATPase activity of WT subunits.

The inhibitory effect of SCN-linked subunits on ATPase activity was more severe. Incorporation of two to four $_{PARL}$Skd3^{N496K} subunits inactivated the hexamer (Figure 7G). Moreover, three to four SCN-linked $_{PARL}$Skd3^{R561G} subunits or four $_{PARL}$Skd3^{R620C} subunits inactivated the hexamer (Figures 7H and S6G). Thus, SCN-linked subunits more sharply inhibit the ATPase activity of WT subunits than MGCA7-linked subunits.

We assessed how MGCA7-linked subunits affected $_{PARL}$Skd3 disaggregase activity in mixing experiments. Six MGCA7-linked $_{PARL}$Skd3^{R408G}, $_{PARL}$Skd3^{R475Q}, or $_{PARL}$Skd3^{A591V} subunits were needed to eliminate $_{PARL}$Skd3 disaggregase activity (Figures 7I, 7J, and S6F). Strikingly, $_{PARL}$Skd3^{A591V} subunits barely affected disaggregase activity even when three mutant subunits were incorporated into the hexamer (Figure S6F). Thus, even one WT $_{PARL}$Skd3 subunit in an otherwise $_{PARL}$Skd3^{R408G}, $_{PARL}$Skd3^{R475Q}, or $_{PARL}$Skd3^{A591V} hexamer enables disaggregase activity. Indeed, MGCA7-linked mutant subunits have only minor effects on the disaggregase activity of WT subunits within the hexamer. The strong buffering activity of WT $_{PARL}$Skd3 subunits explains why MGCA7-linked mutations are biallelic and recessive.

Finally, we assessed how SCN-linked subunits affected $_{PARL}$Skd3 disaggregase activity in mixing experiments (Figures 7K, 7L, and S6H). Incorporation of only two SCN-linked $_{PARL}$Skd3^{N496K} subunits inactivated the hexamer (Figure 7K). Only one or two $_{PARL}$Skd3^{R561G} subunits were required to inactivate the hexamer (Figure 7L). Finally, incorporation of three SCN-linked $_{PARL}$Skd3^{R620C} subunits inactivated the hexamer (Figure S6H). Generally, SCN-linked subunits have a sharper inhibitory effect on WT $_{PARL}$Skd3 than MGCA7-linked subunits (Figures 7E–7L and S6E–S6J). These results explain why SCN-linked mutations are dominant negative and typically monoallelic.

DISCUSSION

Here, we describe $_{PARL}$Skd3 (human *CLPB*) structure and define mechanisms by which $_{PARL}$Skd3 disaggregates proteins. $_{PARL}$Skd3 forms a hexamer with an asymmetric seam between protomers P1 and P6, analogous to other AAA+ proteins, such as Hsp104/ClpB and ClpA (Gates et al., 2017; Lopez et al., 2020; Rizo et al., 2019). $_{PARL}$Skd3 hexamers engage substrate in their central channel via pore-loop interactions in the NBD. Indeed, $_{PARL}$Skd3 may employ a conserved translocation mechanism of other AAA+ translocases (Gates et al., 2017; Puchades et al., 2017; Rizo et al., 2019). Mutation of conserved primary pore-loop residues that engage the substrate (e.g., Y430 and V431) reduce disaggregase activity (Cupo and Shorter, 2020b). Interestingly, mutations at V431 are found in humans (V431D, V431A, and V431I) with low frequency, although none of the known carriers are homozygous (Karczewski et al., 2020). We predict that specific biallelic mutations to V431 would be highly pathogenic.

One of the most prominent features of the $_{PARL}$Skd3 structure is the dodecamer, which is created by two hexamers making head-to-head contacts via the ANK domain. While our paper was under review, it has been independently established that $_{PARL}$Skd3 forms dodecamers (Spaulding et al., 2022; Wu et al., 2022). Moreover, Skd3 forms higher-order structures in cells, consistent with dodecamerization (Thevarajan et al., 2020). The type of dodecameric arrangement formed by $_{PARL}$Skd3 is unusual for a AAA+ protein, but the AAA+ Lon protease can form dodecamers, which exhibit reduced activity for some substrates (Vieux et al., 2013). By contrast, our findings suggest that dodecamer formation may enhance $_{PARL}$Skd3 disaggregase activity. $_{PARL}$Skd3 hexamers and dodecamers are in dynamic equilibrium, but the dodecamer predominates upon polypeptide binding. The head-to-head ANK contacts could concentrate $_{PARL}$Skd3 disaggregases on the aggregate surface and enable stronger pulling forces by maximizing the number of hexamers, simultaneously processing the substrate. Indeed, $_{PARL}$Skd3$^{\Delta L}$, which lacks the ANK linker region, exhibited reduced dodecamerization and reduced disaggregase activity, whereas ATPase activity was unaffected. Moreover, $_{PARL}$Skd3$^{\Delta L507\text{-}I534}$, which lacks the insertion in the NBD, exhibits increased dodecamerization, disaggregase activity, and ATPase activity. Thus, dodecamerization might enhance $_{PARL}$Skd3 disaggregase activity.

The ankyrin repeats are an unusual feature of $_{PARL}$Skd3. The ANK and NBD are required for Skd3 disaggregase activity (Cupo and Shorter, 2020b). Alpha-fold predicts that N-terminal ankyrin repeats 1 and 2 stack on the C-terminal ankyrin repeats 3 and 4, with the largely disordered linker excluded (Figure 3A). Deletion of ankyrin repeats 1 and 2, the linker, or ankyrin repeats 3 and 4 from the ANK reduces disaggregase activity, but not ATPase activity. However, each of these deletion variants retained ~20%–45% $_{PARL}$Skd3 disaggregase activity, indicating that the remaining ankyrin repeats and linker can support some activity. The linker region helps to promote dodecamer formation, whereas deletion of ankyrin repeats 1 and 2 or 3 and 4 does not perturb dodecamerization. The ankyrin repeats likely also play a role in substrate engagement (Wu et al., 2022) or disaggregase plasticity analogous to the Hsp104 N-terminal domain (Sweeny et al., 2015).

Interestingly, several Skd3 transcript variants are found in humans, which differ only in the ANK (The UniProt Consortium, 2021). Residues R152-N180, corresponding to part of ankyrin-repeats 1 and 2, are absent in transcript variant 3. Residues D216-G245, corresponding to the middle section of the linker, are absent in transcript variants 2 and 3. The functional consequences of these transcript variants are not clear, but both deletions correspond to the length of almost exactly one ankyrin repeat (Figure 1A). Thus, cells may tune the level of Skd3 disaggregase activity via translation of these distinct Skd3 transcripts.

Mutant subunit-doping studies suggest that $_{PARL}$Skd3 uses a subglobally cooperative mechanism (i.e., two to five subunits collaborate) to disaggregate disordered luciferase aggregates. $_{PARL}$Skd3 disaggregase activity was very sensitive to mutant subunits that were defective in ATP hydrolysis. Thus, one or two Arg-finger mutant (R561G) subunits, two Walker A mutant (K387A) or sensor-1 mutant (N496K) subunits, or three sensor-2 mutant (R620C) subunits per $_{PARL}$Skd3 hexamer ablated activity. $_{PARL}$Skd3 hexamers exhibit some robustness and can buffer the incorporation of a specific number of mutant subunits, i.e., one subunit with a defective Walker-A motif or sensor-1 motif and two subunits with a defective sensor-2 motif. These results reveal that some AAA+ motifs are more important for subunit cooperativity within the hexamer than others. For example, the Arg finger appears to be more critical than the sensor-2 motif. $_{PARL}$Skd3 hexamers also exhibited robustness against subunits with a defective primary pore loop (Y430A). Thus, $_{PARL}$Skd3 could tolerate four subunits with the Y430A mutation, indicating that two functional pore loops are required for $_{PARL}$Skd3 to maintain a grip on substrate during disaggregation. $_{PARL}$Skd3 differs from Hsp104, which uses a probabilistic mechanism to disaggregate disordered luciferase aggregates (DeSantis et al., 2012).

Skd3 is a therapeutic target to inhibit in prostate cancer and Venetoclax-resistant acute myeloid leukemia (Chen et al., 2019; Pudova et al., 2020). Our structures of $_{PARL}$Skd3 will enable design of small-molecule inhibitors. They are also useful for interpreting disease-linked mutations. SCN-linked mutations cluster within the nucleotide-binding pocket, whereas MGCA7-linked mutations are scattered throughout Skd3. We establish that SCN-linked mutant subunits more sharply inhibit $_{PARL}$Skd3 ATPase and disaggregase activity than MGCA7-linked subunits. The robustness of $_{PARL}$Skd3 against inhibition by MGCA7-linked subunits explains why MGCA7-linked mutations are recessive and must be biallelic to cause disease. Moreover, the sharp

inhibition by SCN-linked mutant subunits explains why SCN-linked mutations are dominant negative.

MGCA7 and SCN are caused by loss-of-function Skd3 mutations (Cupo and Shorter, 2020b; Warren et al., 2022). In principle, both diseases could be treated by increasing Skd3 activity. However, due to the mechanistic differences between how MGCA7-linked and SCN-linked subunits affect activity of WT $_{PARL}$Skd3, different treatment modalities will likely be beneficial for each disease. For treating biallelic MGCA7 mutations, expression of WT Skd3 via adeno-associated viruses (AAVs) is a therapeutic option. Indeed, expression of WT genes via AAVs has yielded therapies for congenital blindness and spinal muscular atrophy (Al-Zaidy et al., 2019; Mendell et al., 2017). Here, the robustness of $_{PARL}$Skd3 hexamers against MGCA7-linked subunits will enable restoration of $_{PARL}$Skd3 activity (Figure S6I). By contrast, SCN-linked mutations are dominant negative, and SCN-linked subunits sharply inhibit WT $_{PARL}$Skd3. Consequently, an AAV strategy to deliver the WT Skd3 gene is likely to be less effective (Figure S6J). We suggest that a therapeutic strategy that reduces or eliminates expression of the mutant Skd3 allele is likely to be more beneficial for SCN. Here, gene editing, specific antisense oligonucleotides, or AAV-delivered siRNA to specifically reduce mutant allele expression could be therapeutic strategies to enable restoration of Skd3 activity.

Limitations of the study

We were unable to resolve a high-resolution structure for the ANK and thus an Alpha -fold model was used. Future studies should solve the atomic structure and dynamics of the ANK. We resolve a $_{PARL}$Skd3 dodecamer that is formed from the head-to-head contact of two hexamers. We establish that the dodecamer exists in solution, but future studies with endogenous substrates and cell models will be needed to further probe the importance of $_{PARL}$Skd3 dodecamers in mitochondria.

STAR★METHODS

Detailed methods are provided in the online version of this paper and include the following:

- KEY RESOURCES TABLE
- RESOURCE AVAILABILITY
  - Lead contact
  - Materials availability
  - Data and code availability
- EXPERIMENTAL MODEL AND SUBJECT DETAILS
- METHOD DETAILS
  - Multiple sequence alignments
  - Purification of $_{PARL}$Skd3
  - Purification of Hsp104
  - Purification of Hsc70 and Hdj1
  - Size-exclusion chromatography
  - Size-exclusion chromatography with multiangle light scattering (SEC-MALS)
  - Cryo-EM data collection and processing for $_{PARL}$Skd3:casein:ATPγS Complex
  - Cryo-EM data collection and processing for $_{PARL}$Skd3$^{\Delta 1\text{-}2}$:casein:ATPγS Complex
  - Molecular modeling
  - ATPase assays
  - Luciferase disaggregation and reactivation assays
  - FITC-casein binding assays
  - Modeling heterohexamer ensemble activity
  - Alexa fluor labeling of $_{PARL}$Skd3
  - Fluorescence resonance energy transfer and subunit mixing
- QUANTIFICATION AND STATISTICAL ANALYSIS

SUPPLEMENTAL INFORMATION

Supplemental information can be found online at https://doi.org/10.1016/j.celrep.2022.111408.

ACKNOWLEDGMENTS

We thank J. Lin, L. Miller, C. Fare, K. Copley, and Z. Tabassum for feedback and the Johnson Foundation Structural Biology and Biophysics Core for SEC-MALS. Our work was funded by a Blavatnik Family Foundation Fellowship (to R.R.C.), The G Harold and Leila Y Mathers Foundation (to J.S.), and NIH grants T32GM008275 (to R.R.C.), F31AG060672 (to R.R.C.), R01GM099836 (to J.S.), R21AG061784 (to J.S.), and R01GM138690 (to D.R.S).

AUTHOR CONTRIBUTIONS

Conceptualization, R.R.C., A.N.R., D.R.S., and J.S.; methodology, R.R.C., A.N.R., G.A.B., E.T., E.C., K.G., D.R.S., and J.S.; validation, R.R.C., A.N.R., G.A.B., E.T., and K.G.; formal analysis, R.R.C., A.N.R., E.C., K.G., D.R.S., and J.S.; investigation, R.R.C., A.N.R., G.A.B., E.T., and K.G.; resources, R.R.C., D.R.S., and J.S.; data curation, R.R.C., A.N.R., D.R.S., and J.S.; writing – original draft, R.R.C., A.N.R., D.R.S., and J.S.; writing – review & editing. R.R.C., A.N.R., G.A.B., E.T., E.C., K.G., D.R.S., and J.S.; visualization, R.R.C., A.N.R., D.R.S., and J.S.; supervision, K.G., D.R.S., and J.S.; project administration, D.R.S. and J.S.; funding acquisition, R.R.C., D.R.S., and J.S.

DECLARATIONS OF INTERESTS

J.S. is a consultant for Dewpoint Therapeutics, Confluence Therapeutics, Neumora, and ADRx.

Received: February 25, 2022
Revised: June 2, 2022
Accepted: September 1, 2022
Published: September 27, 2022

SUPPORTING CITATIONS

The following reference appears in the supplemental information: Lee et al. (2003).

REFERENCES

Al-Zaidy, S.A., Kolb, S.J., Lowes, L., Alfano, L.N., Shell, R., Church, K.R., Nagendran, S., Sproule, D.M., Feltner, D.E., Wells, C., et al. (2019). AVXS-101 (onasemnogene abeparvovec) for SMA1: comparative study with a prospective natural history cohort. J. Neuromuscul. Dis. *6*, 307–317.

Antonicka, H., Lin, Z.Y., Janer, A., Aaltonen, M.J., Weraarpachai, W., Gingras, A.C., and Shoubridge, E.A. (2020). A high-density human mitochondrial proximity interaction network. Cell Metabol. *32*, 479–497.e479.

Botham, A., Coyaud, E., Nirmalanandhan, V.S., Gronda, M., Hurren, R., Maclean, N., St-Germain, J., Mirali, S., Laurent, E., Raught, B., et al. (2019). Global interactome mapping of mitochondrial intermembrane space proteases identifies a novel function for HTRA2. Proteomics *19*, e1900139.

Capo-Chichi, J.M., Boissel, S., Brustein, E., Pickles, S., Fallet-Bianco, C., Nassif, C., Patry, L., Dobrzeniecka, S., Liao, M., Labuda, D., et al. (2015). Disruption of CLPB is associated with congenital microcephaly, severe encephalopathy and 3-methylglutaconic aciduria. J. Med. Genet. *52*, 303–311.

Chen, X., Glytsou, C., Zhou, H., Narang, S., Reyna, D.E., Lopez, A., Sakellaropoulos, T., Gong, Y., Kloetgen, A., Yap, Y.S., et al. (2019). Targeting mitochondrial structure sensitizes acute myeloid leukemia to Venetoclax treatment. Cancer Discov. *9*, 890–909.

Croll, T.I. (2018). ISOLDE: a physically realistic environment for model building into low-resolution electron-density maps. Acta Crystallogr. D Struct. Biol. *74*, 519–530.

Cupo, R.R., and Shorter, J. (2020a). Expression and purification of recombinant Skd3 (human ClpB) protein and tobacco Etch virus (TEV) protease from Escherichia coli. Bio Protoc. *10*, e3858.

Cupo, R.R., and Shorter, J. (2020b). Skd3 (human ClpB) is a potent mitochondrial protein disaggregase that is inactivated by 3-methylglutaconic aciduria-linked mutations. Elife *9*.

Cushman-Nick, M., Bonini, N.M., and Shorter, J. (2013). Hsp104 suppresses polyglutamine-induced degeneration post onset in a Drosophila MJD/SCA3 model. PLoS Genet. *9*, e1003781.

DeSantis, M.E., Leung, E.H., Sweeny, E.A., Jackrel, M.E., Cushman-Nick, M., Neuhaus-Follini, A., Vashist, S., Sochor, M.A., Knight, M.N., and Shorter, J. (2012). Operational plasticity enables Hsp104 to disaggregate diverse amyloid and non-amyloid clients. Cell *151*, 778–793.

Durie, C.L., Lin, J., Scull, N.W., Mack, K.L., Jackrel, M.E., Sweeny, E.A., Castellano, L.M., Shorter, J., and Lucius, A.L. (2019). Hsp104 and potentiated variants can operate as distinct nonprocessive translocases. Biophys. J. *116*, 1856–1872.

Emsley, P., Lohkamp, B., Scott, W.G., and Cowtan, K. (2010). Features and development of Coot. Acta Crystallogr D Biol Crystallogr. *66*, 486–501.

Erives, A., and Fassler, J. (2015). Metabolic and chaperone gene loss marks the origin of animals: evidence for hsp104 and hsp78 chaperones sharing mitochondrial enzymes as clients. PLoS One *10*.

Erzberger, J.P., and Berger, J.M. (2006). Evolutionary relationships and structural mechanisms of AAA+ proteins. Annu. Rev. Biophys. Biomol. Struct. *35*, 93–114.

Fare, C.M., and Shorter, J. (2021). Dis)Solving the problem of aberrant protein states. Dis. Model. Mech. *14*.

Fei, X., Bell, T.A., Jenni, S., Stinson, B.M., Baker, T.A., Harrison, S.C., and Sauer, R.T. (2020). Structures of the ATP-fueled ClpXP proteolytic machine bound to protein substrate. Elife *9*.

Gates, S.N., Yokom, A.L., Lin, J., Jackrel, M.E., Rizo, A.N., Kendsersky, N.M., Buell, C.E., Sweeny, E.A., Mack, K.L., Chuang, E., et al. (2017). Ratchet-like polypeptide translocation mechanism of the AAA+ disaggregase Hsp104. Science *357*, 273–279.

Gellerich, F.N., Laterveer, F.D., Zierz, S., and Nicolay, K. (2002). The quantitation of ADP diffusion gradients across the outer membrane of heart mitochondria in the presence of macromolecules. Biochim. Biophys. Acta *1554*, 48–56.

Glover, J.R., and Lindquist, S. (1998). Hsp104, Hsp70, and Hsp40: a novel chaperone system that rescues previously aggregated proteins. Cell *94*, 73–82.

Grant, T., Rohou, A., and Grigorieff, N. (2018). cisTEM, user-friendly software for single-particle image processing. Elife *7*, e35383.

Grimminger, V., Richter, K., Imhof, A., Buchner, J., and Walter, S. (2004). The prion curing agent guanidinium chloride specifically inhibits ATP hydrolysis by Hsp104. J. Biol. Chem. *279*, 7378–7383.

Hattendorf, D.A., and Lindquist, S.L. (2002). Cooperative kinetics of both Hsp104 ATPase domains and interdomain communication revealed by AAA sensor-1 mutants. EMBO J. *21*, 12–21.

Heldt, H.W., Klingenberg, M., and Milovancev, M. (1972). Differences between the ATP-ADP ratios in the mitochondrial matrix and in the extramitochondrial space. Eur. J. Biochem. *30*, 434–440.

Howard, M.K., Sohn, B.S., von Borcke, J., Xu, A., and Jackrel, M.E. (2020). Functional analysis of proposed substrate-binding residues of Hsp104. PLoS One *15*, e0230198.

Huang, L., Agrawal, T., Zhu, G., Yu, S., Tao, L., Lin, J., Marmorstein, R., Shorter, J., and Yang, X. (2021). DAXX represents a new type of protein-folding enabler. Nature *597*, 132–137.

Hung, V., Zou, P., Rhee, H.W., Udeshi, N.D., Cracan, V., Svinkina, T., Carr, S.A., Mootha, V.K., and Ting, A.Y. (2014). Proteomic mapping of the human mitochondrial intermembrane space in live cells via ratiometric APEX tagging. Mol. Cell *55*, 332–341.

Imamura, H., Nhat, K.P., Togawa, H., Saito, K., Iino, R., Kato-Yamada, Y., Nagai, T., and Noji, H. (2009). Visualization of ATP levels inside single living cells with fluorescence resonance energy transfer-based genetically encoded indicators. Proc. Natl. Acad. Sci. USA *106*, 15651–15656.

Jaru-Ampornpan, P., Shen, K., Lam, V.Q., Ali, M., Doniach, S., Jia, T.Z., and Shan, S.O. (2010). ATP-independent reversal of a membrane protein aggregate by a chloroplast SRP subunit. Nat. Struct. Mol. Biol. *17*, 696–702.

Jackrel, M.E., DeSantis, M.E., Martinez, B.A., Castellano, L.M., Stewart, R.M., Caldwell, K.A., Caldwell, G.A., and Shorter, J. (2014). Potentiated Hsp104 variants antagonize diverse proteotoxic misfolding events. Cell. *156*, 170–182.

Jaru-Ampornpan, P., Liang, F.C., Nisthal, A., Nguyen, T.X., Wang, P., Shen, K., Mayo, S.L., and Shan, S.O. (2013). Mechanism of an ATP-independent protein disaggregase: II. distinct molecular interactions drive multiple steps during aggregate disassembly. J. Biol. Chem. *288*, 13431–13445.

Jumper, J., Evans, R., Pritzel, A., Green, T., Figurnov, M., Ronneberger, O., Tunyasuvunakool, K., Bates, R., Zidek, A., Potapenko, A., et al. (2021). Highly accurate protein structure prediction with AlphaFold. Nature *596*, 583–589.

Kanabus, M., Shahni, R., Saldanha, J.W., Murphy, E., Plagnol, V., Hoff, W.V., Heales, S., and Rahman, S. (2015). Bi-allelic CLPB mutations cause cataract, renal cysts, nephrocalcinosis and 3-methylglutaconic aciduria, a novel disorder of mitochondrial protein disaggregation. J. Inherit. Metab. Dis. *38*, 211–219.

Karczewski, K.J., Francioli, L.C., Tiao, G., Cummings, B.B., Alfoldi, J., Wang, Q., Collins, R.L., Laricchia, K.M., Ganna, A., Birnbaum, D.P., et al. (2020). The mutational constraint spectrum quantified from variation in 141,456 humans. Nature *581*, 434–443.

Kiykim, A., Garncarz, W., Karakoc-Aydiner, E., Ozen, A., Kiykim, E., Yesil, G., Boztug, K., and Baris, S. (2016). Novel CLPB mutation in a patient with 3-methylglutaconic aciduria causing severe neurological involvement and congenital neutropenia. Clin. Immunol. *165*, 1–3.

Klosowska, A., Chamera, T., and Liberek, K. (2016). Adenosine diphosphate restricts the protein remodeling activity of the Hsp104 chaperone to Hsp70 assisted disaggregation. Elife *5*.

Kohl, A., Binz, H.K., Forrer, P., Stumpp, M.T., Pluckthun, A., and Grutter, M.G. (2003). Designed to be stable: crystal structure of a consensus ankyrin repeat protein. Proc. Natl. Acad. Sci. USA *100*, 1700–1705.

Lee, S., Sowa, M.E., Watanabe, Y., Sigler, P.B., Chiu, W., Yoshida, M., and Tsai, F.T.F. (2003). The structure of ClpB: a molecular chaperone that rescues proteins from an aggregated state. Cell. *115*, 229–240.

Liebschner, D., Afonine, P.V., Baker, M.L., Bunkoczi, G., Chen, V.B., Croll, T.I., Hintze, B., Hung, L.W., Jain, S., McCoy, A.J., et al. (2019). Macromolecular structure determination using X-rays, neutrons and electrons: recent developments in Phenix. Acta Crystallogr. D Struct. Biol. *75*, 861–877.

Lin, J., Shorter, J., and Lucius, A.L. (2022). AAA+ proteins: one motor, multiple ways to work. Biochem. Soc. Trans. *50*, 895–906.

Lo Bianco, C., Shorter, J., Regulier, E., Lashuel, H., Iwatsubo, T., Lindquist, S., and Aebischer, P. (2008). Hsp104 antagonizes alpha-synuclein aggregation and reduces dopaminergic degeneration in a rat model of Parkinson disease. J. Clin. Invest. *118*, 3087–3097.

Lopez, K.E., Rizo, A.N., Tse, E., Lin, J., Scull, N.W., Thwin, A.C., Lucius, A.L., Shorter, J., and Southworth, D.R. (2020). Conformational plasticity of the ClpAP AAA+ protease couples protein unfolding and proteolysis. Nat. Struct. Mol. Biol. *27*, 406–416.

Mackay, R.G., Helsen, C.W., Tkach, J.M., and Glover, J.R. (2008). The C-terminal extension of Saccharomyces cerevisiae Hsp104 plays a role in oligomer assembly. Biochemistry *47*, 1918–1927.

Madeira, F., Park, Y.M., Lee, J., Buso, N., Gur, T., Madhusoodanan, N., Basutkar, P., Tivey, A.R.N., Potter, S.C., Finn, R.D., et al. (2019). The EMBL-EBI search and sequence analysis tools APIs in 2019. Nucleic Acids Res. *47*, W636–W641.

McGeoch, A.T., Trakselis, M.A., Laskey, R.A., and Bell, S.D. (2005). Organization of the archaeal MCM complex on DNA and implications for the helicase mechanism. Nat. Struct. Mol. Biol. *12*, 756–762.

Mendell, J.R., Al-Zaidy, S., Shell, R., Arnold, W.D., Rodino-Klapac, L.R., Prior, T.W., Lowes, L., Alfano, L., Berry, K., Church, K., et al. (2017). Single-dose gene-replacement therapy for spinal muscular atrophy. N. Engl. J. Med. *377*, 1713–1722.

Michalska, K., Zhang, K., March, Z.M., Hatzos-Skintges, C., Pintilie, G., Bigelow, L., Castellano, L.M., Miles, L.J., Jackrel, M.E., Chuang, E., et al. (2019). Structure of calcarisporiella thermophila Hsp104 disaggregase that antagonizes diverse proteotoxic misfolding events. Structure *27*, 449–463.e447.

Moreau, M.J., McGeoch, A.T., Lowe, A.R., Itzhaki, L.S., and Bell, S.D. (2007). ATPase site architecture and helicase mechanism of an archaeal MCM. Mol. Cell *28*, 304–314.

Mosavi, L.K., Cammett, T.J., Desrosiers, D.C., and Peng, Z.Y. (2004). The ankyrin repeat as molecular architecture for protein recognition. Protein Sci. *13*, 1435–1448.

Mosavi, L.K., Minor, D.L., Jr., and Peng, Z.Y. (2002). Consensus-derived structural determinants of the ankyrin repeat motif. Proc. Natl. Acad. Sci. USA *99*, 16029–16034.

Mroz, D., Wyszkowski, H., Szablewski, T., Zawieracz, K., Dutkiewicz, R., Bury, K., Wortmann, S.B., Wevers, R.A., and Zietkiewicz, S. (2020). CLPB (caseinolytic peptidase B homolog), the first mitochondrial protein refoldase associated with human disease. Biochim. Biophys. Acta Gen. Subj. *1864*, 129512.

Parra, R.G., Espada, R., Verstraete, N., and Ferreiro, D.U. (2015). Structural and energetic characterization of the ankyrin repeat protein family. PLoS Comput. Biol. *11*, e1004659.

Perier, F., Radeke, C.M., Raab-Graham, K.F., and Vandenberg, C.A. (1995). Expression of a putative ATPase suppresses the growth defect of a yeast potassium transport mutant: identification of a mammalian member of the Clp/HSP104 family. Gene *152*, 157–163.

Pettersen, E.F., Goddard, T.D., Huang, C.C., Couch, G.S., Greenblatt, D.M., Meng, E.C., and Ferrin, T.E. (2004). UCSF Chimera–a visualization system for exploratory research and analysis. J. Comput. Chem. *25*, 1605–1612.

Pettersen, E.F., Goddard, T.D., Huang, C.C., Meng, E.C., Couch, G.S., Croll, T.I., Morris, J.H., and Ferrin, T.E. (2021). UCSF ChimeraX: structure visualization for researchers, educators, and developers. Protein Sci. *30*, 70–82.

Pronicka, E., Ropacka-Lesiak, M., Trubicka, J., Pajdowska, M., Linke, M., Ostergaard, E., Saunders, C., Horsch, S., van Karnebeek, C., Yaplito-Lee, J., et al. (2017). A scoring system predicting the clinical course of CLPB defect based on the foetal and neonatal presentation of 31 patients. J. Inherit. Metab. Dis. *40*, 853–860.

Puchades, C., Rampello, A.J., Shin, M., Giuliano, C.J., Wiseman, R.L., Glynn, S.E., and Lander, G.C. (2017). Structure of the mitochondrial inner membrane AAA+ protease YME1 gives insight into substrate processing. Science *358*.

Puchades, C., Sandate, C.R., and Lander, G.C. (2020). The molecular principles governing the activity and functional diversity of AAA+ proteins. Nat. Rev. Mol. Cell Biol. *21*, 43–58.

Pudova, E.A., Krasnov, G.S., Kobelyatskaya, A.A., Savvateeva, M.V., Fedorova, M.S., Pavlov, V.S., Nyushko, K.M., Kaprin, A.D., Alekseev, B.Y., Trofimov, D.Y., et al. (2020). Gene expression changes and associated pathways involved in the progression of prostate cancer advanced stages. Front. Genet. *11*, 613162.

Punjani, A., Rubinstein, J.L., Fleet, D.J., and Brubaker, M.A. (2017). cryoSPARC: algorithms for rapid unsupervised cryo-EM structure determination. Nat. Methods *14*, 290–296.

Rath, S., Sharma, R., Gupta, R., Ast, T., Chan, C., Durham, T.J., Goodman, R.P., Grabarek, Z., Haas, M.E., Hung, W.H.W., et al. (2021). MitoCarta3.0: an updated mitochondrial proteome now with sub-organelle localization and pathway annotations. Nucleic Acids Res. *49*, D1541–D1547.

Rhee, H.W., Zou, P., Udeshi, N.D., Martell, J.D., Mootha, V.K., Carr, S.A., and Ting, A.Y. (2013). Proteomic mapping of mitochondria in living cells via spatially restricted enzymatic tagging. Science *339*, 1328–1331.

Rizo, A.N., Lin, J., Gates, S.N., Tse, E., Bart, S.M., Castellano, L.M., DiMaio, F., Shorter, J., and Southworth, D.R. (2019). Structural basis for substrate gripping and translocation by the ClpB AAA+ disaggregase. Nat. Commun. *10*, 2393.

Saita, S., Nolte, H., Fiedler, K.U., Kashkar, H., Venne, A.S., Zahedi, R.P., Kruger, M., and Langer, T. (2017). PARL mediates Smac proteolytic maturation in mitochondria to promote apoptosis. Nat. Cell Biol. *19*, 318–328.

Saunders, C., Smith, L., Wibrand, F., Ravn, K., Bross, P., Thiffault, I., Christensen, M., Atherton, A., Farrow, E., Miller, N., et al. (2015). CLPB variants associated with autosomal-recessive mitochondrial disorder with cataract, neutropenia, epilepsy, and methylglutaconic aciduria. Am. J. Hum. Genet. *96*, 258–265.

Schirmer, E.C., Queitsch, C., Kowal, A.S., Parsell, D.A., and Lindquist, S. (1998). The ATPase activity of Hsp104, effects of environmental conditions and mutations. J. Biol. Chem. *273*, 15546–15552.

Shivhare, D., Ng, J., Tsai, Y.C., and Mueller-Cajar, O. (2019). Probing the rice Rubisco-Rubisco activase interaction via subunit heterooligomerization. Proc. Natl. Acad. Sci. USA *116*, 24041–24048.

Shorter, J., and Southworth, D.R. (2019). Spiraling in control: structures and mechanisms of the Hsp104 disaggregase. Cold Spring Harb. Perspect. Biol. *11*.

Skokowa, J., Dale, D.C., Touw, I.P., Zeidler, C., and Welte, K. (2017). Severe congenital neutropenias. Nat. Rev. Dis Primers *3*, 17032.

Spaulding, Z., Thevarajan, I., Schrag, L.G., Zubcevic, L., Zolkiewska, A., and Zolkiewski, M. (2022). Human mitochondrial AAA+ ATPase SKD3/CLPB assembles into nucleotide-stabilized dodecamers. Biochem. Biophys. Res. Commun. *602*, 21–26.

Spinazzi, M., Radaelli, E., Horre, K., Arranz, A.M., Gounko, N.V., Agostinis, P., Maia, T.M., Impens, F., Morais, V.A., Lopez-Lluch, G., et al. (2019). PARL deficiency in mouse causes Complex III defects, coenzyme Q depletion, and Leigh-like syndrome. Proc. Natl. Acad. Sci. USA *116*, 277–286.

Sweeny, E.A., Jackrel, M.E., Go, M.S., Sochor, M.A., Razzo, B.M., DeSantis, M.E., Gupta, K., and Shorter, J. (2015). The Hsp104 N-terminal domain enables disaggregase plasticity and potentiation. Mol. Cell *57*, 836–849.

The UniProt Consortium (2021). UniProt: the universal protein knowledgebase in 2021. Nucleic Acids Res. *49*, D480–D489.

Thevarajan, I., Zolkiewski, M., and Zolkiewska, A. (2020). Human CLPB forms ATP-dependent complexes in the mitochondrial intermembrane space. Int. J. Biochem. Cell Biol. *127*, 105841.

Varadi, M., Anyango, S., Deshpande, M., Nair, S., Natassia, C., Yordanova, G., Yuan, D., Stroe, O., Wood, G., Laydon, A., et al. (2022). AlphaFold Protein Structure Database: massively expanding the structural coverage of protein-sequence space with high-accuracy models. Nucleic Acids Res. *50*, D439–D444.

Vieux, E.F., Wohlever, M.L., Chen, J.Z., Sauer, R.T., and Baker, T.A. (2013). Distinct quaternary structures of the AAA+ Lon protease control substrate degradation. Proc. Natl. Acad. Sci. USA *110*, E2002–E2008.

Wang, R.Y., Song, Y., Barad, B.A., Cheng, Y., Fraser, J.S., and DiMaio, F. (2016). Automated structure refinement of macromolecular assemblies from cryo-EM maps using Rosetta. Elife *5*, e17219.

Warren, J.T., Cupo, R.R., Wattanasirakul, P., Spencer, D.H., Locke, A.E., Makaryan, V., Bolyard, A.A., Kelley, M.L., Kingston, N.L., Shorter, J., et al. (2022). Heterozygous variants of CLPB are a cause of severe congenital neutropenia. Blood *139*, 779–791.

Waterhouse, A., Bertoni, M., Bienert, S., Studer, G., Tauriello, G., Gumienny, R., Heer, F.T., de Beer, T.A.P., Rempfer, C., Bordoli, L., et al. (2018). SWISS-MODEL: homology modelling of protein structures and complexes. Nucleic Acids Res. *46*, W296–W303.

Weaver, C.L., Duran, E.C., Mack, K.L., Lin, J., Jackrel, M.E., Sweeny, E.A., Shorter, J., and Lucius, A.L. (2017). Avidity for polypeptide binding by nucleotide-bound Hsp104 structures. Biochemistry *56*, 2071–2075.

Werbeck, N.D., Schlee, S., and Reinstein, J. (2008). Coupling and dynamics of subunits in the hexameric AAA+ chaperone ClpB. J. Mol. Biol. *378*, 178–190.

Wortmann, S.B., Zietkiewicz, S., Kousi, M., Szklarczyk, R., Haack, T.B., Gersting, S.W., Muntau, A.C., Rakovic, A., Renkema, G.H., Rodenburg, R.J., et al. (2015). CLPB mutations cause 3-methylglutaconic aciduria, progressive brain atrophy, intellectual disability, congenital neutropenia, cataracts, movement disorder. Am. J. Hum. Genet. *96*, 245–257.

Wortmann, S.B., Zietkiewicz, S., Guerrero-Castillo, S., Feichtinger, R.G., Wagner, M., Russell, J., Ellaway, C., Mroz, D., Wyszkowski, H., Weis, D., et al. (2021). Neutropenia and intellectual disability are hallmarks of biallelic and de novo CLPB deficiency. Genet. Med. *23*, 1705–1714.

Wu, D., Liu, Y., Dai, Y., Wang, G., Lu, G., Chen, Y., Li, N., Lin, J., and Gao, N. (2022). Structure and mechanism of a mitochondrial AAA+ disaggregase CLBP. Preprint at bioRxiv. https://doi.org/10.1101/2022.03.10.483744.

Yoo, H., Bard, J.A.M., Pilipenko, E.V., and Drummond, D.A. (2022). Chaperones directly and efficiently disperse stress-triggered biomolecular condensates. Mol. Cell *82*, 741–755.e711.

Zheng, S.Q., Palovcak, E., Armache, J.P., Verba, K.A., Cheng, Y., and Agard, D.A. (2017). MotionCor2: anisotropic correction of beam-induced motion for improved cryo-electron microscopy. Nat. Methods *14*, 331–332.

Zhu, G., Harischandra, D.S., Ghaisas, S., Zhang, P., Prall, W., Huang, L., Maghames, C., Guo, L., Luna, E., Mack, K.L., et al. (2020). TRIM11 prevents and reverses protein aggregation and rescues a mouse model of Parkinson's disease. Cell Rep. *33*, 108418.

STAR★METHODS

KEY RESOURCES TABLE

REAGENT or RESOURCE	SOURCE	IDENTIFIER
Bacterial and virus strains		
Escherichia coli BL21-CodonPlus (DE3) -RIL competent cells	Agilent	Cat#230245
Chemicals, peptides, and recombinant proteins		
Creatine phosphate	Roche	Cat#10621722001
Adenosine-5′-Diphosphate Monosodium Salt (ADP)	MP Biomedicals	Cat#150260
Adenylyl-imidodiphosphate (AMP-PNP)	Roche	Cat#10102547001
Adenosine 5′-triphosphate disodium salt hydrate (ATP)	Sigma-Aldrich	Cat#A3377
Adenosine-5′-o-(3-thio-triphosphate) (ATPγS)	Roche	Cat#10102342001
cOmplete, Mini, EDTA-free Protease Inhibitor Cocktail	Sigma-Aldrich	Cat#4693159001
Pepstatin A, microbial, ≥90% (HPLC)	Sigma-Aldrich	Cat#P5318
Alexa Fluor™ 488 NHS Ester (Succinimidyl Ester)	ThermoFisher Scientific	Cat#A20000
Alexa Fluor™ 594 NHS Ester (Succinimidyl Ester)	ThermoFisher Scientific	Cat#A20004
Casein fluorescein isothiocyanate from bovine milk (FITC-Casein)	Sigma-Aldrich	Cat#C0528
Creatine kinase	Roche	Cat#10127566001
Firefly luciferase	Sigma-Aldrich	Cat#L9506
Lysozyme	Sigma-Aldrich	Cat#L6876
His-TEV protease	(Cupo and Shorter, 2020a, b)	N/A
Hdj1	(Cupo and Shorter, 2020b; Michalska et al., 2019)	N/A
Hsc70	(Cupo and Shorter, 2020b; Michalska et al., 2019)	N/A
Hsp104	(DeSantis et al., 2012; Jackrel et al., 2014)	N/A
$_{PARL}$Skd3	(Cupo and Shorter, 2020a, b)	N/A
$_{PARL}$Skd3^{V431G}	This paper	N/A
$_{PARL}$Skd3^{R417A}	This paper	N/A
$_{PARL}$Skd3^{NBD}	(Cupo and Shorter, 2020b)	N/A
$_{PARL}$Skd3$^{\Delta 1\text{-}2}$	This paper	N/A
$_{PARL}$Skd3$^{\Delta L}$	This paper	N/A
$_{PARL}$Skd3$^{\Delta 3\text{-}4}$	This paper	N/A
$_{PARL}$Skd3$^{\Delta L507\text{-}I534}$	This paper	N/A
$_{PARL}$Skd3$^{\Delta L660\text{-}I707}$	This paper	N/A
$_{PARL}$Skd3^{K387A}	(Cupo and Shorter, 2020b)	N/A
$_{PARL}$Skd3^{Y430A}	(Cupo and Shorter, 2020b)	N/A
$_{PARL}$Skd3^{R408G}	(Warren et al., 2022)	N/A
$_{PARL}$Skd3^{R475Q}	(Cupo and Shorter, 2020b)	N/A
$_{PARL}$Skd3^{A591V}	(Cupo and Shorter, 2020b)	N/A
$_{PARL}$Skd3^{N496K}	(Warren et al., 2022)	N/A
$_{PARL}$Skd3^{R561G}	(Warren et al., 2022)	N/A
$_{PARL}$Skd3$^{R62\circ C}$	(Warren et al., 2022)	N/A
Critical commercial assays		
ATPase Activity Kit (Colorimetric)	Innova Biosciencens	Cat#601–0120
Luciferase Assay Reagent	Promega	Cat#E1483
Deposited data		
EMDB: 26121	This paper	N/A
EMDB: 26122	This paper	N/A

(*Continued on next page*)

Continued

REAGENT or RESOURCE	SOURCE	IDENTIFIER
PDB: 7TTR	This paper	N/A
PDB: 7TTS	This paper	N/A
Recombinant DNA		
pHis-TEV	(Cupo and Shorter, 2020a, b)	N/A
pE-SUMO-Hdj1	(Cupo and Shorter, 2020b; Michalska et al., 2019)	N/A
pE-SUMO-Hsc70	(Cupo and Shorter, 2020b; Michalska et al., 2019)	N/A
pNOTAG-Hsp104	(DeSantis et al., 2012; Jackrel et al., 2014)	N/A
pMAL-C2-TEV-$_{PARL}$Skd3	(Cupo and Shorter, 2020a, b)	N/A
pMAL-C2-TEV-$_{PARL}$Skd3^{V431G}	This paper	N/A
pMAL-C2-TEV-$_{PARL}$Skd3^{R417A}	This paper	N/A
pMAL-C2-TEV-$_{PARL}$Skd3^{NBD}	(Cupo and Shorter, 2020b)	N/A
pMAL-C2-TEV-$_{PARL}$Skd3$^{\Delta 1\text{-}2}$	This paper	N/A
pMAL-C2-TEV-$_{PARL}$Skd3$^{\Delta L}$	This paper	N/A
pMAL-C2-TEV-$_{PARL}$Skd3$^{\Delta 3\text{-}4}$	This paper	N/A
pMAL-C2-TEV-$_{PARL}$Skd3$^{\Delta L507\text{-}I534}$	This paper	N/A
pMAL-C2-TEV-$_{PARL}$Skd3$^{\Delta L660\text{-}I707}$	This paper	N/A
pMAL-C2-TEV-$_{PARL}$Skd3^{K387A}	(Cupo and Shorter, 2020b)	N/A
pMAL-C2-TEV-$_{PARL}$Skd3^{Y430A}	(Cupo and Shorter, 2020b)	N/A
pMAL-C2-TEV-$_{PARL}$Skd3^{R408G}	(Warren et al., 2022)	N/A
pMAL-C2-TEV-$_{PARL}$Skd3^{R475Q}	(Cupo and Shorter, 2020b)	N/A
pMAL-C2-TEV-$_{PARL}$Skd3^{A591V}	(Cupo and Shorter, 2020b)	N/A
pMAL-C2-TEV-$_{PARL}$Skd3^{N496K}	(Warren et al., 2022)	N/A
pMAL-C2-TEV-$_{PARL}$Skd3^{R561G}	(Warren et al., 2022)	N/A
pMAL-C2-TEV-$_{PARL}$Skd3$^{R62\circ C}$	(Warren et al., 2022)	N/A
Software and algorithms		
BOXSHADE	Github	https://github.com/mdbaron42/pyBoxshade
Clustal Omega	(Madeira et al., 2019)	N/A
Prism 8	GraphPad	N/A
ASTRA, version 8.0	Wyatt Technology	N/A
cryoSPARC version 2.0–3.3.2	Structura Biotechnology Inc.	N/A
Chimera	(Pettersen et al., 2004)	N/A
ChimeraX version 1.2.5–1.3	(Pettersen et al., 2021)	N/A
ISOLDE	(Croll, 2018)	N/A
cisTEM	(Grant et al., 2018)	N/A
Phenix (Phenix Real Space Refine)	(Liebschner et al., 2019)	N/A
Coot	(Emsley et al., 2010)	N/A
Rosetta (2020.08 Release)	(Wang et al., 2016)	N/A
AlphaFold	(Jumper et al., 2021; Varadi et al., 2022)	N/A

RESOURCE AVAILABILITY

Lead contact

Further information and requests for resources and reagents should be directed to and will be fulfilled by the lead contact, James Shorter (jshorter@pennmedicine.upenn.edu).

Materials availability

Plasmids newly generated in this study will be made readily available to the scientific community. We will honor requests in a timely fashion. Material transfers will be made with no more restrictive terms than in the Simple Letter Agreement or the Uniform Biological Materials Transfer Agreement and without reach through requirements.

Data and code availability

- $_{PARL}$Skd3:casein:ATPγS cryo-EM maps and atomic coordinates have been deposited in the EMDB and PDB with accession codes EMDB: 26121 (State 1), EMDB: 26122 (State 1 filtered), PDB: 7TTR (State 1, AAA + only), and PDB: 7TTS (State 1, Full Model). The original/source data in the paper are available from the lead contact upon reasonable request.
- This paper did not generate code.
- Any additional information required to reanalyze the data reported in this paper is available from the lead contact upon request.

EXPERIMENTAL MODEL AND SUBJECT DETAILS

Escherichia coli BL21-CodonPlus (DE3)-RIL competent cells (Genotype: B F– ompT hsdS(rB – mB –) dcm + Tetr gal l (DE3) endA Hte [argU ileY leuW Camr) (Agilent, Cat#230245) were used to express recombinant proteins for purification.

METHOD DETAILS

Multiple sequence alignments

NBD sequences were acquired via UniProtKB for *Homo sapiens* Skd3, *Escherichia coli* ClpA, *Escherichia coli* ClpB, *Staphylococcus aureus* ClpC, *Escherichia coli* ClpX, *Saccharomyces cerevisiae* Hsp78, *Arabidopsis thaliana* Hsp101, *Saccharomyces cerevisiae* Hsp104, *Escherichia coli* RuvB, and *Pseudomonas aeruginosa* ClpG. Ankyrin-repeat sequences were acquired via UniProtKB for *Homo sapiens* Skd3. Consensus ankyrin repeat was derived from Mosavi, et al. (Mosavi et al., 2002). Compiled sequences were aligned via Clustal Omega (Madeira et al., 2019). The linker region of the ankyrin repeats was aligned manually to the Clustal Omega alignment. Alignment image was generated via BoxShade tool as described previously (Cupo and Shorter, 2020b).

Purification of $_{PARL}$Skd3

$_{PARL}$Skd3 and variants were purified as previously described (Cupo and Shorter, 2020a, b). In short, $_{PARL}$Skd3 and variants were expressed with an N-terminal MBP-tag in BL21 (DE3) RIL cells (Agilent). Cells were lysed via sonication in lysis buffer (40 mM HEPES-KOH pH = 7.4, 500 mM KCl, 20% [w/v] glycerol, 5 mM ATP, 10 mM $MgCl_2$, 2 mM β-mercaptoethanol, 2.5 μM PepstatinA, and cOmplete Protease Inhibitor Cocktail [one tablet/250 mL, Millipore Sigma]). Lysates were cleared via centrifugation at 30,597xg and 4°C for 20 min and the supernatant was applied to amylose resin (NEB). The column was washed with 15 column volumes (CV) of wash buffer (WB: 40 mM HEPES-KOH pH = 7.4, 500 mM KCl, 20% [w/v] glycerol, 5 mM ATP, 10 mM $MgCl_2$, 2 mM β-mercaptoethanol, 2.5 μM PepstatinA, and cOmplete Protease Inhibitor Cocktail [1 full size tablet/50mL, Millipore Sigma]) at 4°C, 3 CV of WB supplemented with 20 mM ATP at 25°C for 30 min, and an additional 15 CV of WB at 4°C. The protein was then washed with ~8 CV of elution buffer (EB: 50 mM Tris-HCl pH = 8.0, 300 mM KCl, 10% glycerol, 5 mM ATP, 10 mM $MgCl_2$, and 2 mM β-mercaptoethanol) and eluted via TEV protease cleavage at 34°C. The protein was run over a size exclusion column (GE Healthcare HiPrep 26/60 Sephacryl S-300 HR) in sizing buffer (50 mM Tris-HCl pH = 8.0, 500 mM KCl, 10% glycerol, 1 mM ATP, 10 mM $MgCl_2$, and 1 mM DTT). Peak fractions were collected, concentrated to ~5 mg/mL, supplemented with 5 mM ATP, and snap frozen. Protein purity was determined to be >95% by SDS-PAGE and Coomassie staining.

Purification of Hsp104

Hsp104 was purified as previously described (DeSantis et al., 2012). In short, Hsp104 was expressed in BL21 (DE3) RIL cells, lysed via sonication in lysis buffer (50 mM Tris-HCl pH = 8.0, 10 mM $MgCl_2$, 2.5% glycerol, 2 mM β-mercaptoethanol, 2.5 μM PepstatinA, and cOmplete Protease Inhibitor Cocktail [one mini EDTA-free tablet/50 mL, Millipore Sigma]), centrifuged at 30,597xg and 4°C for 20 min, and purified on Affi-Gel Blue Gel (Bio-Rad). Hsp104 was eluted in elution buffer (50 mM Tris-HCl pH = 8.0, 1M KCl, 10 mM $MgCl_2$, 2.5% glycerol, and 2 mM β-mercaptoethanol) and then exchanged into storage buffer (40 mM HEPES-KOH pH = 7.4, 500 mM KCl, 20 mM MgCl2, 10% glycerol, 1 mM DTT). The protein was diluted to 10% in buffer Q (20 mM Tris-HCl pH = 8.0, 50 mM NaCl, 5 mM $MgCl_2$, and 0.5 mM EDTA) and loaded onto a 5 mL RESOURCE Q anion exchange chromatography (GE Healthcare). Hsp104 was eluted via linear gradient of buffer Q+ (20 mM Tris pH = 8.0, 1M NaCl, 5 mM $MgCl_2$, and 0.5 mM EDTA). The protein was exchanged into storage buffer and snap frozen. Protein purity was determined to be >95% by SDS-PAGE and Coomassie staining.

Purification of Hsc70 and Hdj1

Hsc70 and Hdj1 were purified as previously described (Michalska et al., 2019). Hsc70 and Hdj1 were expressed in BL21 (DE3) RIL cells with an N-terminal His-SUMO tag. Cells were lysed via sonication into lysis buffer (50 mM HEPES-KOH pH = 7.5, 750 mM KCl, 5 mM $MgCl_2$, 10% glycerol, 20 mM imidazole, 2 mM β-mercaptoethanol, 5 μM pepstatin A, and cOmplete Protease Inhibitor Cocktail [one mini EDTA-free tablet/50 mL, Millipore Sigma]). Lysates were cleared via centrifugation at 30,597xg and 4°C for 20 min. The supernatant was bound to Ni-NTA Agarose resin (Qiagen), washed with 10 CV of wash buffer (50 mM HEPES-KOH pH = 7.5, 750 mM KCl, 10 mM $MgCl_2$, 10% glycerol, 20 mM imidazole, 1 mM ATP, and 2 mM β-mercaptoethanol), and eluted with 2 CV of elution buffer (wash buffer supplemented with 300 mM imidazole). The tag was removed via Ulp1 (1:100 Ulp1:Protein molar ratio) cleavage during dialysis into wash buffer. The protein was further purified via loading onto a 5 mL HisTrap HP column (GE Healthcare)

and pooling the untagged elution. The protein was pooled and concentrated, and then purified further via Resource Q ion-exchange chromatography. The elution was pooled, concentrated, and snap frozen. Protein purity was determined to be >95% via SDS-PAGE and Coomassie staining.

Size-exclusion chromatography

All size-exclusion chromatography experiments were run on a Superose 6 Increase 3.2/300 (Cytiva) column pre-equilibrated in buffer containing: 40 mM HEPES (pH = 8.0), 40 mM KCl, 10 $MgCl_2$, and 1 mM DTT. To form a substrate-bound complex, $_{PARL}$Skd3 (20 μM) was incubated with FITC-casein (55 μM) (#C0528; Sigma) in the presence of nucleotide (ATPγS, ATP, ADP, or AMP-PNP) (5 mM) for 15 min at room temperature. For experiments without FITC-casein, $_{PARL}$Skd3 (20 μM) and nucleotide (ATPγS, ATP, ADP, or AMP-PNP) (5 mM) were incubated for 15 min at room temperature. After the incubation period, the samples were spin-filtered before injecting on column.

Size-exclusion chromatography with multiangle light scattering (SEC-MALS)

Experiments were conducted at the Johnson Foundation Structural Biology and Biophysics Core at the Perelman School of Medicine (Philadelphia, PA). The SEC experiments were performed using 100 μL injections (125μM $_{PARL}$Skd3) with a Superose 6 Increase 10/300 GL column (GE Life Sciences) at 0.5 mL/min at room temperature. The column was equilibrated with 20 mM Tris-HCl (pH = 8.00), 150 mM KCl, and 10 mM $MgCl_2$ and 1 mM DTT at 25°C. Absolute molecular weights were determined by MALS. The scattered light intensity of the column eluent was recorded at 18 different angles using a DAWN-HELEOS MALS detector (Wyatt Technology Corporation) operating at 658 nm after calibration with the monomer fraction of Type V BSA (Sigma). The protein concentration of the eluent was determined using an in-line Optilab T-rex interferometric refractometer (Wyatt Technology Corporation). The weight-averaged molecular weight of species within defined chromatographic peaks was calculated using the software ASTRA, version 8.0 (Wyatt Technology Corporation), by construction of Debye plots [(KC/Rθ versus sin2(θ/2)] at 1/S data intervals. The weight-averaged molecular weight was then calculated at each point of the chromatographic trace from the Debye plot intercept, and an overall average molecular weight was calculated by averaging across the peak.

Cryo-EM data collection and processing for $_{PARL}$Skd3:casein:ATPγS Complex

To form a substrate-bound complex, $_{PARL}$Skd3 (55 μM) was incubated with FITC-casein (55 μM) (#C0528; Sigma) in the presence of ATPγS (5 mM) in buffer containing: 40 mM HEPES (pH = 8.0), 40 mM KCl, 10 $MgCl_2$, 1 mM DTT. After incubating for 15 min at room temperature, the sample was applied to a Superose 6 Increase 3.2/300 column (GE Healthcare) for size exclusion chromatography (SEC) analysis. The fraction corresponding to the largest molecular weight complex from SEC of $_{PARL}$Skd3 and FITC-casein (Figure 1B) was isolated and incubated with 1 mM ATPγS. Before freezing, proper dilutions were made to a final concentration of ∼.7 mg/mL and a 3.0 μL drop was applied to glow discharged holey carbon (R 1.2/1.3; Quantifoil), then blotted for 3 s at 4°C and 100% humidity with a blot force of 1, followed by an additional 3.0μL drop. The sample was then blotted again for 2 s with a blot force of 0 with Whatman No. 1 filter paper before being plunge frozen in liquid ethane using a Vitrobot (Thermo Fischer Scientific).

The sample was then imaged on a Titan Krios TEM (Thermo Fischer Scientific) operated at 300 keV and equipped with a Gatan BioQuantum imaging energy filter using a 20eV zero loss energy slit (Gatan Inc). Movies were acquired in super-resolution mode on a K3 direct electron detector (Gatan Inc.) at a nominal magnification of 105,000X corresponding to a physical pixel size of 0.417 Å/pixel. A defocus range of 0.8–1.2 μm was used with a total exposure time of 2 s fractionated into 0.2s subframes for a total dose of 68 e−/$Å^2$ at a dose rate of 25 e−/pixel/s. Movies were subsequently corrected for drift using MotionCor2 (Zheng et al., 2017) and were Fourier cropped by a factor of 2 to a final pixel size of 0.834 Å/pixel.

A total of ∼30,000 micrographs were collected over multiple datasets. Micrograph quality was assessed and poor micrographs, including those above the resolution cutoff of ∼5Å, were discarded. The individual datasets were processed separately to ensure data quality before combining them all together for further processing. Data processing was performed in cryoSPARC v3.2 (Punjani et al., 2017). For particle picking, blob picker was set to 180 Å-200 Å for minimum and maximum particle diameter and the particles picked were inspected before extracting particles. 2D classification was performed to remove contamination and junk particles and good classes were selected which left ∼900,000 remaining particles. Four different ab-initio models were reconstructed which were then used in 3D classification.

Heterogeneous refinement was performed with 4 different classes, which resulted in 3 distinct classes: hexamer, Class 1 (41%, ∼358K particles); heptamer, Class 3 (19%, ∼167K particles); and dodecamer, Class 2 (15%, ∼130K particles); Other, Class 4 (24%, ∼210K particles) (Figure S1F). Each of the classes underwent homogeneous refinement which resulted in resolutions of 9Å for the dodecamer, 7 Å for the heptamer and 3.2Å for the hexamer. To improve the resolution, non-uniform refinement was completed on both the dodecamer and hexamer to improve the resolutions to 7.2Å and 2.9Å respectively (Figure S2B). Both classes underwent local CTF refinement which did not result in an improvement in resolution.

Cryo-EM data collection and processing for $_{PARL}$Skd3$^{Δ1-2}$:casein:ATPγS Complex

To form a substrate-bound complex, $_{PARL}$Skd3$^{Δ1-2}$ (40 μM) was incubated with FITC-casein (40 μM) (#C0528; Sigma) in the presence of ATPγS (5 mM) in buffer containing: 40 mM HEPES (pH = 8.0), 40 mM KCl, 10 $MgCl_2$, 1 mM DTT. After incubating for 15 min at room temperature, grids were prepared. For grid freezing, a 3.0 μL drop was applied to glow discharged holey carbon (R 1.2/1.3;

Quantifoil), then blotted for 3 s at 4°C and 100% humidity with a blot force of 1 followed by an additional 3.0μL drop. The sample was then blotted again for 2 s with a blot force of 0 with Whatman No. 1 filter paper before being plunge frozen in liquid ethane using a Vitrobot (Thermo Fischer Scientific).

The sample was then imaged on a Glacios TEM (Thermo Fischer Scientific) operated at 200 keV (Gatan Inc). Movies were acquired in super-resolution mode on a K2 direct electron detector (Gatan Inc.) at a nominal magnification of ,45,000X corresponding to a physical pixel size of 0.486 Å/pixel. A defocus range of 1.0–2.0 μm was used with a total exposure time of 6 s fractionated into 0.06s subframes for a total dose of 55.8 e−/Å^2 at a dose rate of 8 e−/pixel/s. Movies were subsequently corrected for drift using MotionCor2 (Zheng et al., 2017) and were Fourier cropped by a factor of 2 to a final pixel size of 0.972 Å/pixel.

A total of ~15,000 micrographs were collected over multiple datasets. The individual datasets were processed separately to ensure data quality before combining them all together for further processing. Micrograph quality was assessed and poor micrographs, including those above the resolution cutoff of ~5Å, were discarded. Data processing was performed in cryoSPARC v3.2 (Punjani et al., 2017). For particle picking, blob picker was set to 180 Å-200 Å for minimum and maximum particle diameter and the particles picked were inspected before extracting particles. 2D classification was performed in two rounds to remove contamination and junk particles and good classes were selected which left ~700,000 remaining particles. The results from a previous 3D classification were used as the starting models for 3D classification.

Heterogeneous refinement was performed with 4 different classes, which resulted in 3 distinct classes: dodecamer, Class 1 (24%, ~165K particles); bent dodecamer, Class 2 (30%, ~203K particles); trimer, Class 3 (32%, ~213K particles); and other, Class 4 (14%, ~95K particles) (Figure S3I). Each of the classes underwent homogeneous refinement which resulted in resolutions of 8Å for the dodecamer, 7Å for the bent dodecamer and 8Å for the trimer (Figure S3J).

Molecular modeling

An initial model for $_{PARL}$Skd3was generated in SWISS-MODEL (Waterhouse et al., 2018) and was docked into the EM map using the UCSF chimera's function fit in map (Pettersen et al., 2004). The initial model lacked the ANK so the SWISS-MODEL generated was combined with the Alpha-fold prediction of the ANK taken from the AlphaFold Protein Structure Database. Initial refinement was performed using Rosetta_Relax in cartesian space to generate 30 different models. The map/model quality for each model generated was examined in Chimera (Pettersen et al., 2004) and the lowest energy minimized model was used moving forward. Various outliers and poorly fit density were manually fixed using ISOLDE (Croll, 2018) in ChimeraX (Pettersen et al., 2021). To fix most of the outliers another round of Rosetta_Relax in cartesian space was performed followed by iterative rounds of refinement in Phenix Real Space Refine (Liebschner et al., 2019). The model from Phenix Real Space refinement was taken and used in a final round of Rosetta FastRelax in torsion space to remove the various clashes that were introduced during Phenix refinement.

ATPase assays

Hsp104, $_{PARL}$Skd3, and $_{PARL}$Skd3 variants (0.25 μM monomer) were incubated with ATP (1 mM) (Innova Biosciences) at 37°C for 5 min in luciferase reactivation buffer (LRB; 25 mM HEPES-KOH [pH = 8.0], 150 mM KAOc, 10 mM MgAOc, 10 mM DTT). ATPase activity was assessed via inorganic phosphate release with a malachite green detection assay (Expedeon) and measured in Nunc 96 Well Optical plates on a Tecan Infinite M1000 plate reader. Background hydrolysis was measured at time zero and subtracted (Cupo and Shorter, 2020b; DeSantis et al., 2012). ATPase kinetics for $_{PARL}$Skd3 were calculated using GraphPad Prism with a Michaelis-Menten least squares fit which was subsequently used to derive K_M and V_{max}.

Luciferase disaggregation and reactivation assays

Firefly luciferase was aggregated by incubating luciferase (50 μM) in LRB (pH = 7.4) with 8M urea at 30°C for 30 min. The denatured luciferase was then rapidly diluted 100-fold into ice-cold LRB, snap frozen, and stored at −80°C until use. Hsp104 (1μM monomer) was incubated with 50 nM aggregated firefly luciferase in the presence or absence of Hsc70 and Hdj2 (0.167 μM each) in LRB plus 5 mM ATP plus an ATP regeneration system (ARS; 1 mM creatine phosphate and 0.25 μM creatine kinase) at 37°C for 90 min (unless otherwise indicated). $_{PARL}$Skd3 and variants (1 μM monomer, unless otherwise indicated) were incubated with 50 nM aggregated firefly luciferase in LRB plus 5 mM ATP plus ARS at 37°C for 90 min (unless otherwise indicated). Nucleotide-inhibitor assays for $_{PARL}$Skd3 disaggregation activity were tested in the presence of ATP (Sigma), ATPγS (Roche), or ADP (MP Biomedicals) for 30 min at 37°C without ARS. IC_{50} curves for ADP and ATPγS were fitted using GraphPad Prism with a variable slope (four parameters) least squares fit. Recovered luminescence was monitored in Nunc 96 Well Optical plates using a Tecan Infinite M1000 plate reader (Cupo and Shorter, 2020b; DeSantis et al., 2012; Glover and Lindquist, 1998). Typically, Hsp104, Hsc70, and Hdj2 recovered ~10% of native luciferase activity, whereas $_{PARL}$Skd3 recovered ~45% native luciferase activity (Cupo and Shorter, 2020b). Under our conditions, neither ADP nor ATPγS had an inhibitory effect on native luciferase (Figure 5).

FITC-casein binding assays

Fluorescence polarization was performed essentially as described previously (Rizo et al., 2019). $_{PARL}$Skd3 was exchanged into 40 mM HEPES-KOH pH 8.0, 20 mM $MgCl_2$, 150 mM KCl, 10% Glycerol (v/v), 2 mM β-mercaptoethanol. To assess FITC-casein binding, FITC-casein (60 nM, Sigma) was incubated with increasing concentrations (0-2.5μM hexameric) of $_{PARL}$Skd3 with 2 mM of the indicated nucleotide for 10 min at 25°C. For the ATP condition, an ATP regeneration system (5 mM creatine phosphate and 0.125 μM

creatine kinase) was included to maintain 2 mM ATP. Fluorescence polarization was measured (excitation 470 nm, emission 520 nm) using a Tecan Infinite M1000 plate reader. The binding isotherms were analyzed using Prism.

Modeling heterohexamer ensemble activity

The binomial distribution was used to model the activity of various heterohexamer ensembles (DeSantis et al., 2012; Werbeck et al., 2008):

$$P(k) = \binom{n}{k} p^k (1-p)^{n-k}$$

Where: P(k) is the probability of a hexamer containing k mutant subunits, n is total number of subunits (which for a hexamer, n = 6), and p is the probability that a mutant subunit is incorporated. FRET subunit mixing experiments demonstrated that mutant and WT subunits have a similar probability of being incorporated into a hexamer (Figures S5D, 6A and 6B). Thus, p is calculated as the molar ratio of mutant and WT protein present:

$$p = Skd3^{mutant} \left(Skd3^{mutant} + Skd3^{WT} \right)$$

Therefore, for any specified concentration of mutant protein, the probability distribution of $_{PARL}$Skd3 hexamers containing zero, one, two, three, four, five, or six mutant subunits can be derived (Figure 6A). Activity versus p plots (Figure 6B) can then be generated assuming each WT subunit makes an equal contribution to the total activity (one-sixth per subunit). Consequently, if subunits within the hexamer operate independently then activity should decline linearly upon incorporation of mutant subunits. Conversely, if subunit activity is coupled then the incorporation of a specific number of subunits will be sufficient to abolish activity. In our model, zero activity is assigned to hexamers that exceed the specific threshold number of mutant subunits. In this way, we generate activity versus p plots by assuming that 1 or more, 2 or more, 3 or more, 4 or more, or 5 or more mutant subunits are required to eliminate activity. This formula can be expressed as:

$$Activity\ (\%) = 100 * [(P_0A_0) + (P_1A_1) + (P_2A_2) + (P_3A_3) + (P_4A_4) + (P_5A_5) + (P_6A_6)]$$

Where: P(k) is the probability of hexamer containing k mutant subunits derived above and A(k) is the relative assigned contribution to activity of a hexamer containing k mutant subunits.

Alexa fluor labeling of $_{PARL}$Skd3

For Förster resonance energy transfer (FRET) studies, we labeled separate pools of $_{PARL}$Skd3 with Alexa Fluor 488 (Alexa 488, ThermoFisher Scientific CAT# A20000) as the FRET donor and Alexa Fluor 594 (Alexa 594, ThermoFisher Scientific CAT# A20004) as the FRET acceptor. In brief, $_{PARL}$Skd3 (WT and mutants) was extensively exchanged into labeling buffer (LB; 50 mM HEPES-KOH [pH = 8.0], 150 mM KCl, 20 mM $MgCl_2$, 10% glycerol, 10mM BME) at room temperature using Micro Bio-Spin 6 columns (Bio-Rad CAT# 7326200). $_{PARL}$Skd3 concentration was measured via A280 and the molar extinction coefficient and $_{PARL}$Skd3 concentration was adjusted to 30 μM. The primary amine (R-NH2) reactive dye, Alexa Fluor 488 NHS Ester (Succinimidyl Ester) (Alexa 488) or Alexa Fluor 594 NHS Ester (Succinimidyl Ester) (Alexa 594), was then added to $_{PARL}$Skd3 samples to achieve a 10-fold molar excess over $_{PARL}$Skd3. Samples were then incubated at 25°C in the dark. After 75min, the labeling reaction was quenched by rapidly and extensively exchanging into labeling buffer +10 mM DTT. To ensure that all unreacted dye is removed, the buffer exchange step was repeated at least twice. $_{PARL}$Skd3 concentration and labeling efficiency were determined by UV/Vis spectrometry according to the manufacturer's instructions (Invitrogen). Typically, we achieved ~50% labeling efficiency.

Fluorescence resonance energy transfer and subunit mixing

We employed Förster resonance energy transfer (FRET) to measure subunit mixing (Figures S5D, 6A and 6B). Donor (Alexa Fluor 488) labeled $_{PARL}$Skd3 (Alexa 488- $_{PARL}$Skd3), Acceptor (Alexa Fluor 594) labeled $_{PARL}$Skd3 (Alexa 594-$_{PARL}$Skd3), or free dye were mixed in equal stoichiometric parts to a final total dye concentration of 1μM in labeling buffer with ATP (5 mM). Because these dyes function as an FRET pair with a Förster radius of 60 Å, primary amine labeling in $_{PARL}$Skd3 is expected to yield intermolecular FRET once mixed oligomers are formed. Given the R_0 value of 60Å for the Alexa 488-Alexa594 FRET pair, it is possible to observe both intrahexameric FRET (e.g. solvent exposed residues K538 from P3 and K658 from P4 are 8.5 Å apart) and interhexameric FRET within a dodecamer (closest two lysines are K134 to K265 at 22.4 Å apart, but it is unclear if they are solvent exposed). However, the hexameric state is the predominant species in the absence of substrate and thus our FRET assay likely reports on the hexameric state of $_{PARL}$Skd3 rather than the dodecamer (Figure 1B). A similar strategy has been employed to demonstrate the formation of mixed hexamers by bacterial ClpB (Werbeck et al., 2008), Hsp104 (DeSantis et al., 2012), and MCM helicase, another AAA + ATPase, from *Sulfolobus solfataricus* (McGeoch et al., 2005; Moreau et al., 2007). Prior to any measurements, samples were allowed to equilibrate for 10 min at room temperature. Mixed and equilibrated samples were excited at the donor excitation wavelength of 480nm. Donor fluorescence was measured at 519nm with a bandwidth of 5nm. Acceptor fluorescence was measured at 630nm with a bandwidth of 5nm. Apparent FRET efficiency (Figures S5D, S6C and S6D) was calculated from Alexa 488-$_{PARL}$Skd3 emission (488nm) and Alexa 594-$_{PARL}$Skd3

emission (519nm) as $F_a/(F_d + F_a)$, where F_d is the measured Alexa 488-$_{PARL}$Skd3 (donor) fluorescence and F_a is the Alexa 594-$_{PARL}$Skd3 (acceptor) fluorescence in the presence of Alexa 488-Skd3.

QUANTIFICATION AND STATISTICAL ANALYSIS

Quantification is as described in the figure legends. Statistical analyses were performed using the GraphPad Prism (GraphPad Software, Inc,; La Jolla, CA, USA) as described in figure legends.

Cell Reports, Volume *40*

Supplemental information

Unique structural features govern the activity of a human mitochondrial AAA+ disaggregase, Skd3

Ryan R. Cupo, Alexandrea N. Rizo, Gabriel A. Braun, Eric Tse, Edward Chuang, Kushol Gupta, Daniel R. Southworth, and James Shorter

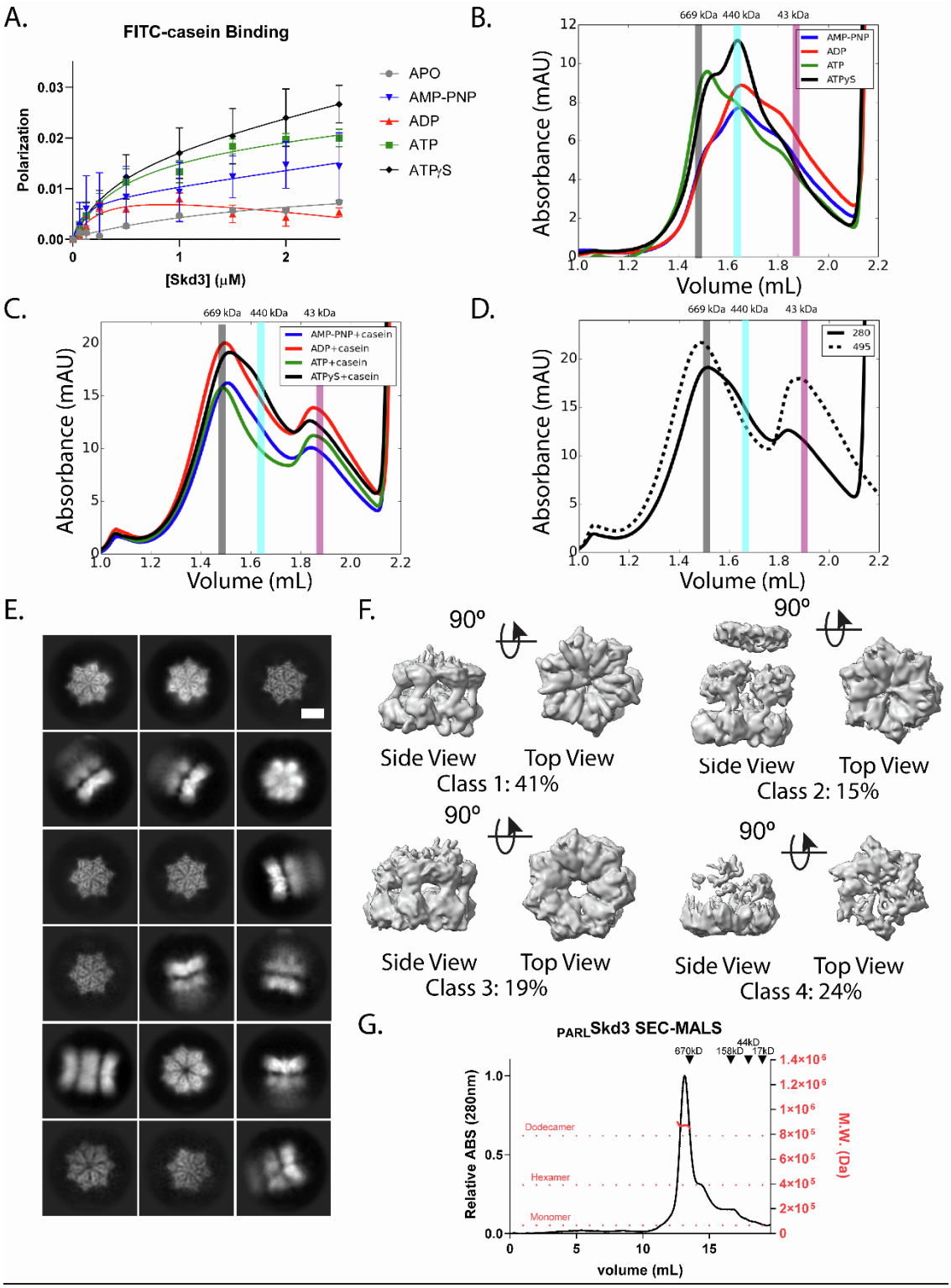

Figure S1. Structure of $_{PARL}$Skd3. (A) FITC-casein binding analysis, measured by fluorescence polarization in the presence of no nucleotide (APO; grey), AMP-PNP (blue), ADP (red), ATP (green), and ATPγS (black). Values represent means ± SEM (n=3). **(B, C)** SEC-trace of

$_{PARL}$Skd3 with different nucleotides without casein **(B)** and with casein **(C)** including AMP-PNP (blue), ADP (red), ATP (green), and ATPγS (black). The three vertical bars represent different molecular weight standards thyroglobulin (669 kDa), ferritin (440 kDa), and ovalbumin (43 kDa) that approximately represent Skd3 dodecamers (grey), hexamers (cyan), or monomers (magenta). **(D)** SEC-trace of $_{PARL}$Skd3:casein:ATPγS complex with both 280nm UV absorbance (solid) and 495nm UV absorbance to detect FITC-casein (dashed) shown. Vertical bars indicate molecular-weight standards as in Figure S1B. **(E)** Representative 2D class averages from the full dataset. Scale bar, 100Å. **(F)** 3D classification results from the total combined dataset: hexamer, Class 1 (top, left); dodecamer, Class 2 (top, right); heptamer, Class 3 (bottom, left); and other, Class 4 (bottom, right). **(G)** SEC-MALS identifies the presence of dodecameric $_{PARL}$Skd3 in solution. Left y-axis label and black circle traces represent relative protein concentration determined by relative absorbance at 280 nm (A280). Elution peaks for sizing standards are demarked with black triangles. Right y-axis label and hollow red circle traces represent molecular weight readings as measured by multi-angle light scattering. Red horizontal dashed lines demark the theoretical molecular weights of monomeric, hexameric, and dodecameric $_{PARL}$Skd3.
Related to Figure 1.

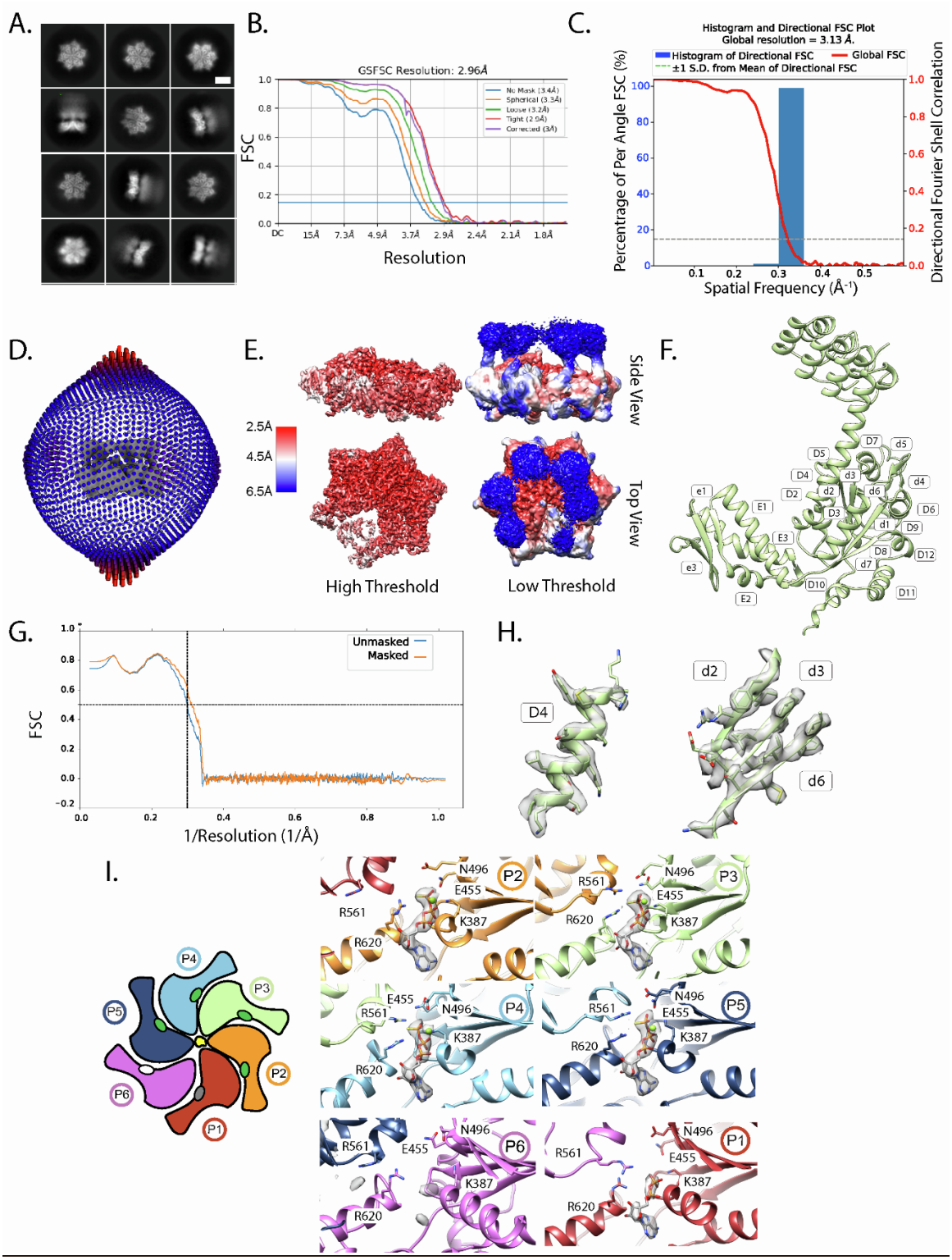

Figure S2. Structure and nucleotide-binding pockets of $_{PARL}$Skd3. (A) Representative 2D class averages from the hexamer class. Scale bar, 100Å. **(B)** Gold standard FSC-curves for the hexamer class refinement. **(C)** Histogram and directional FSC plot for the hexamer class. **(D)**

Particle distribution map of the dodecamer class. **(E)** Local resolution map of the hexamer map and two different threshold high threshold (left) and low threshold (right). **(F)** PARLSkd3 structure labeled for reference with NBD helices and strands indicated for the large subdomain (D) or small subdomain (E) as for NBD2 of bacterial ClpB (PDB: 1QVR) (Lee et al., 2003). **(G)** Map vs. Model FSC for both unmasked (blue) and masked (orange) for the hexamer model. **(H)** Map plus model of alpha helix, D4, and beta-sheets d2, d3, and d6. **(I)** Schematic of NBD structure (top view) with circles representing ATP (green), ADP (grey), or APO (white) in the nucleotide-binding pocket (left). Map and model of the nucleotide-binding pocket with residues involved in ATP hydrolysis are shown and labeled including Arg Finger (R561), sensor-1 (N496), sensor-2 (R620), Walker A (K387), and Walker B (E455) (right).
Related to Figure 1 and 2.

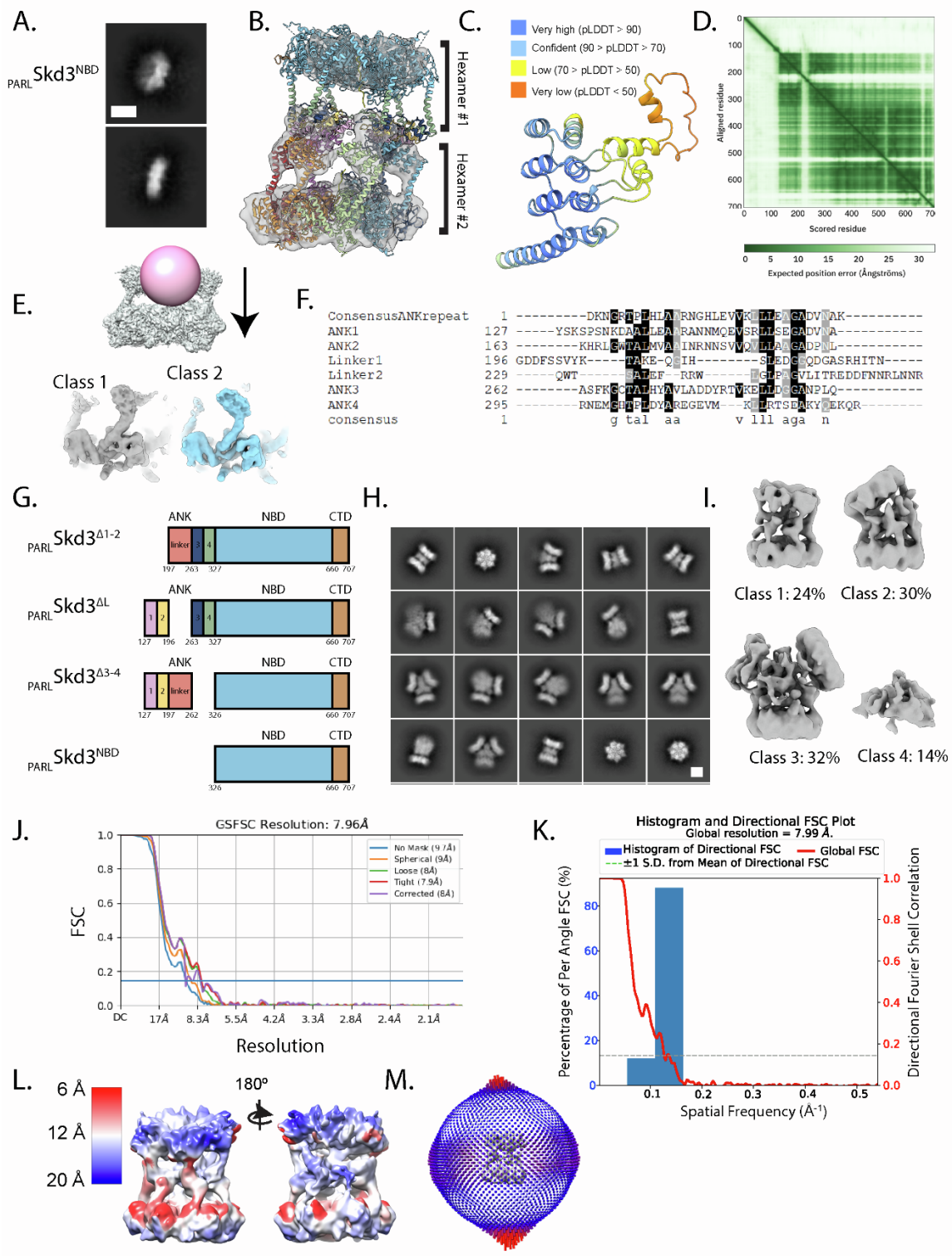

Figure S3. Structural refinement of the ANK. (A) Representative 2D class averages from $_{PARL}$Skd3^{NBD}. Scale bar, 100Å. **(B)** Dodecamer map of $_{PARL}$Skd3 from 3D classification with representative model colored by individual domains docked in the top hexamer. The bottom

hexamer is colored by protomer. **(C)** Model prediction from Alpha-Fold of ANK colored by pLDDDT score. **(D)** Plot of the predicted aligned error of the Alpha-Fold prediction of full length Skd3. **(E)** Mask (pink) and map (grey) used in focus classification in cisTEM (Grant et al., 2018) of the single ankyrin domain on the hexamer class (left) with results of two representative classes (right). **(F)** Alignment of the four ankyrin repeats and the linker region of *H. sapiens* Skd3 to the consensus ankyrin repeat from Mosavi, *et. al.* (Mosavi et al., 2002). Alignments were constructed using Clustal Omega. Linker region was aligned to consensus sequence manually. Bottom row shows consensus sequence of alignment. **(G)** Domain architecture maps of the different ANK deletion mutations. **(H)** Representative 2D class averages from the $_{PARL}$Skd3$^{\Delta 1\text{-}2}$ dataset. Scale bar, 100Å. **(I)** 3D classification results from the $_{PARL}$Skd3$^{\Delta 1\text{-}2}$ dataset: dodecamer, Class 1 (left); bent dodecamer, Class 2 (middle left); trimer, Class 3 (middle right); and other, Class 4 (right). **(J)** Gold standard FSC-curves for the final dodecamer class refinement. **(K)** Histogram and directional FSC plot for the dodecamer class. **(L)** Local resolution map of the dodecamer map. **(M)** Particle distribution map of the dodecamer class. Related to Figure 3.

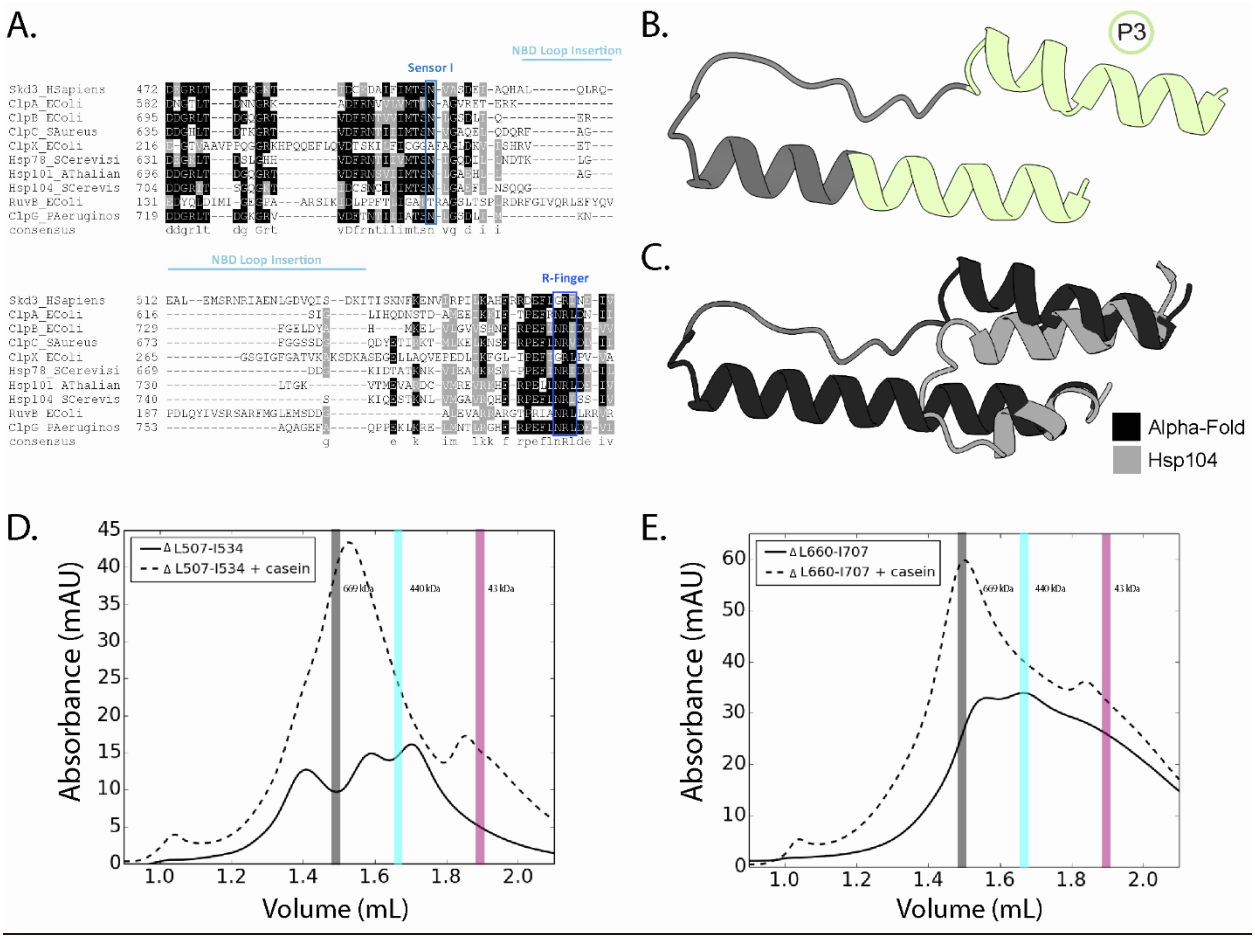

Figure S4. Structural features of the NBD insertion and CTD. (A) Alignment of a select region of the NBD from *H. sapiens* Skd3, NBD2 from *E. coli* ClpA, NBD2 from *E. coli* ClpB, NBD2 from *A. aureus* ClpC, NBD from *E. coli* ClpX, NBD2 from *S. cerevisiae* Hsp78, NBD2 from *A. thaliana* Hsp101, NBD2 from *S. cerevisiae* Hsp104, NBD from *E. coli* RuvB, and NBD2 from *P. aeruginosa* ClpG. Alignments were constructed using Clustal Omega. Bottom row shows consensus sequence of alignment. Highlighted in blue are the sensor-1 and Arg-finger motifs. Light blue highlights the insertion from L507-I534 in the Skd3 NBD. **(B)** Alpha-fold model prediction (grey) of the NBD insertion alone (residues 449-515 to 535-552 are shown). The residues that were successfully built in de novo are represented in green on the model of protomer 3. **(C)** The Alpha-fold model prediction (black) overlayed with the Hsp104 model (grey, PDB: 5VJH). **(D)** SEC of $_{PARL}$Skd3$^{\Delta L507\text{-}I534}$ plus ATPSγS with casein (dashed) and without casein (solid). The three vertical bars represent different molecular weight standards thyroglobulin (669 kDa), ferritin (440 kDa), and ovalbumin (43 kDa) that approximately represent Skd3 dodecamers (grey), hexamers (cyan), or monomers (magenta). **(E)** SEC of

$_{PARL}$Skd3$^{\Delta L660\text{-}I707}$ plus ATPSγS with casein (dashed) and without casein (solid). The three vertical bars represent different molecular weight standards thyroglobulin (669 kDa), ferritin (440 kDa), and ovalbumin (43 kDa) that approximately represent Skd3 dodecamers (grey), hexamers (cyan), or monomers (magenta).

Related to Figure 4.

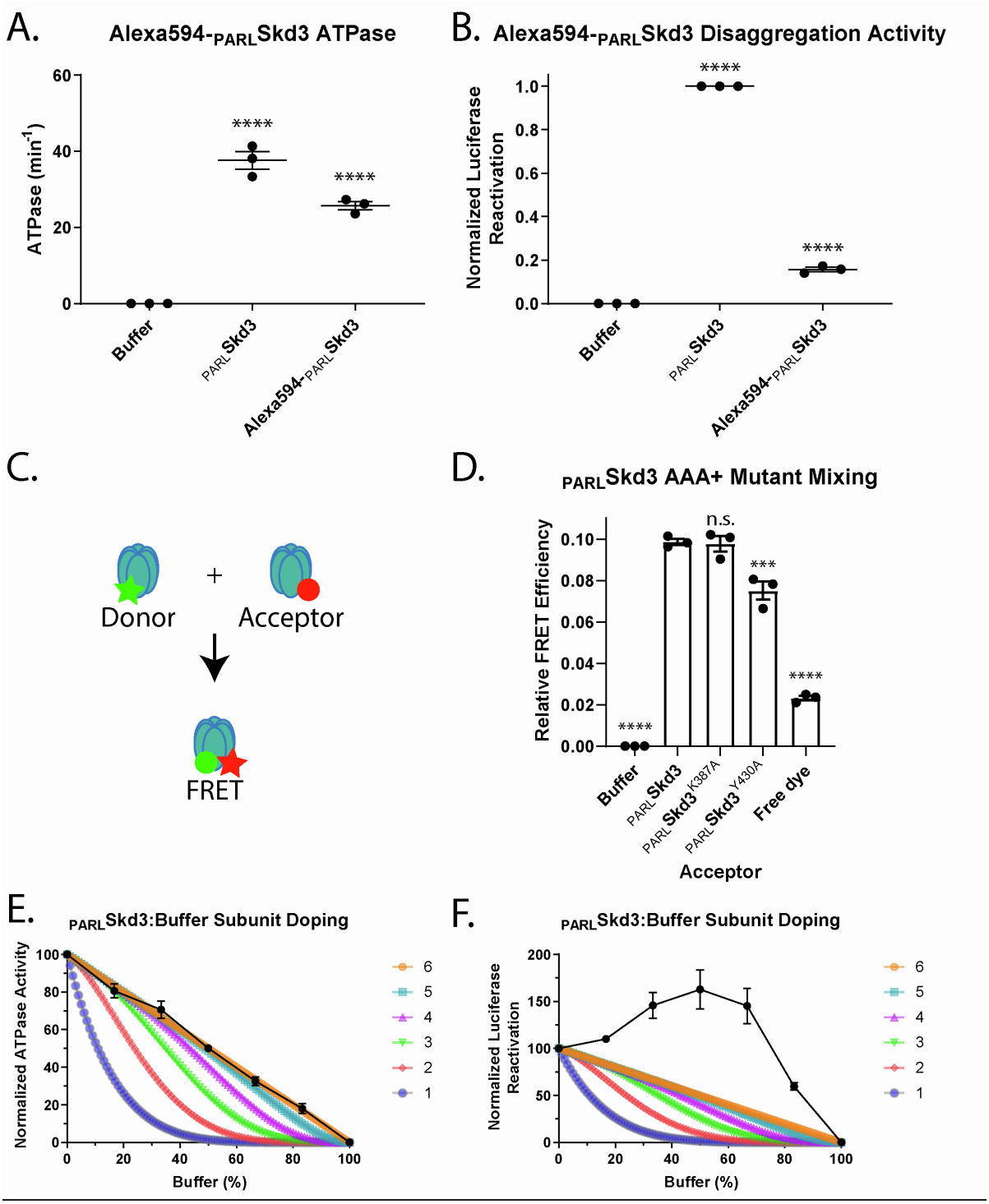

Figure S5. Skd3 is a subglobally cooperative protein disaggregase. (A) ATPase activity of PARLSkd3 and Alexa594-PARLSkd3. ATPase activity was compared to buffer using one-way ANOVA and a Dunnett's multiple comparisons test (n = 3, individual data points shown as dots, bars show mean ± SEM, ****p<0.0001). **(B)** Luciferase disaggregase activity of PARLSkd3 and

Alexa594-$_{PARL}$Skd3. Luciferase activity was buffer subtracted and normalized to $_{PARL}$Skd3. Disaggregase activity was compared to buffer using one-way ANOVA and a Dunnett's multiple comparisons test (n = 3, individual data points shown as dots, bars show mean ± SEM, ****p<0.0001). **(C)** Schematic of subunit mixing assayed by FRET. Separate pools of $_{PARL}$Skd3 were labeled with Alexa-Fluor 488 (Alexa488) to serve as a donor and Alexa-Fluor 594 (Alexa594) to serve as an acceptor. In mixed hexamers, the donor (Alexa488) and acceptor (Alexa594) labels come into close enough proximity to elicit FRET. **(D)** FRET efficiency after mixing Alexa488-$_{PARL}$Skd3 with buffer, Alexa594-$_{PARL}$Skd3, Alexa594-$_{PARL}$Skd3^{K387A}, Alexa594-$_{PARL}$Skd3^{E455Q}, or Alexa594-$_{PARL}$Skd3^{Y430A} for 10 min in the presence of ATP (5 mM) at a 1:1 molar ratio with a final labelled $_{PARL}$Skd3 concentration of 1μM. As a negative control the FRET efficiency of mixing unreacted Alexa488 dye with unreacted Alexa594 dye is also shown. Relative FRET efficiency was compared to WT $_{PARL}$Skd3 using one-way ANOVA and a Dunnett's multiple comparisons test (n = 3, individual data points shown as dots, bars show mean ± SEM, ****p<0.0001). **(E)** ATPase activity of $_{PARL}$Skd3 mixed with various ratios of buffer. ATPase activity was buffer subtracted and normalized to $_{PARL}$Skd3 (n = 3, data shown as black dots with mean ± SEM). **(F)** Luciferase disaggregase activity of $_{PARL}$Skd3 mixed with various ratios of buffer. Disaggregase activity was buffer subtracted and normalized to $_{PARL}$Skd3 (n = 3, data shown as black dots with mean ± SEM).
Related to Figure 6.

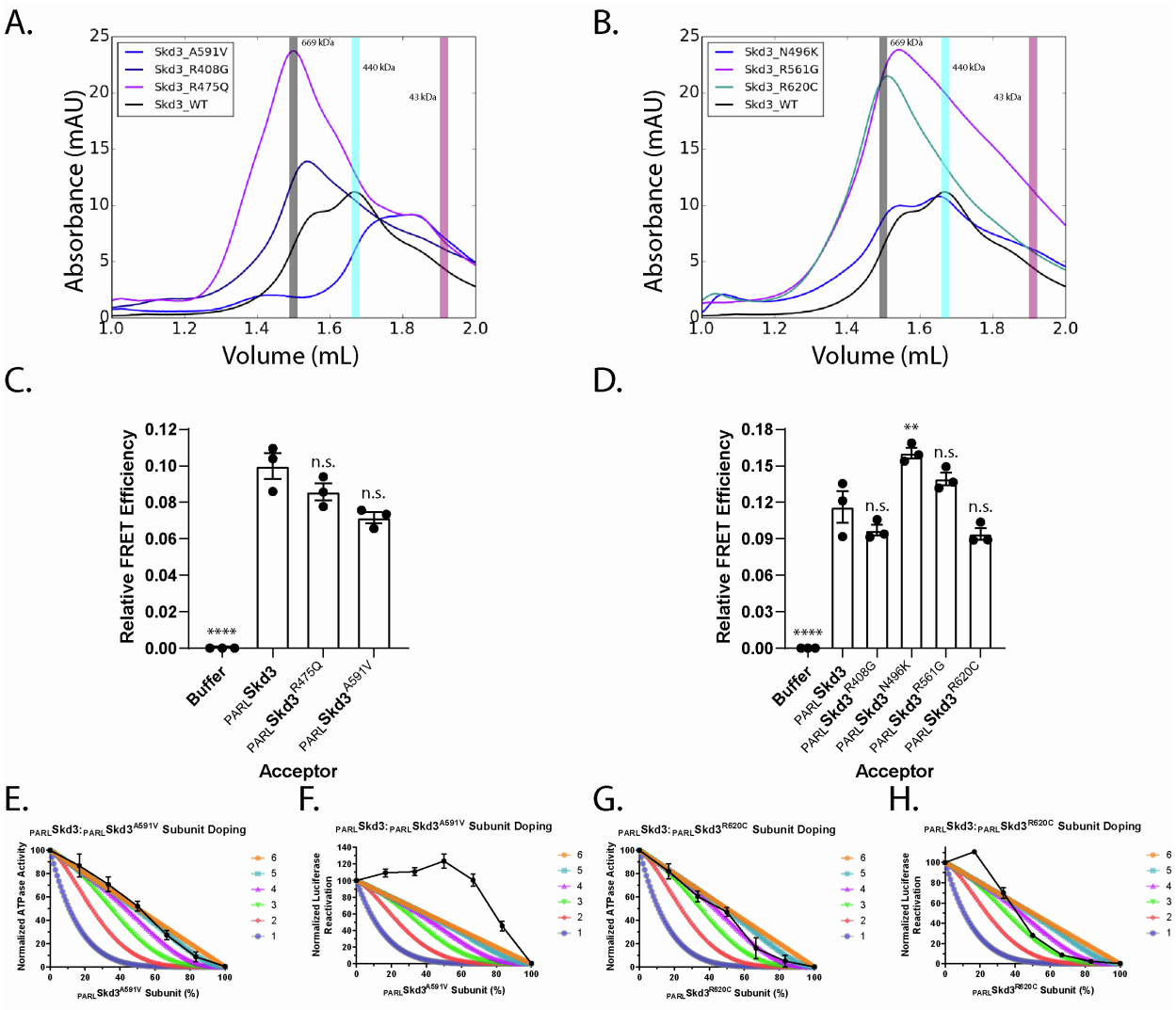

I.

	Number of subunits required to inactivate hexamer	
	ATPase	Disaggregase
PARLSkd3R408G	6	6
PARLSkd3R475Q	6	6
PARLSkd3A591V	5	6

J.

	Number of subunits required to inactivate hexamer	
	ATPase	Disaggregase
PARLSkd3N496K	2-4	2
PARLSkd3R561G	3-4	1-2
PARLSkd3R620C	3-4	3

Figure S6. SCN-linked subunits inhibit $_{PARL}$Skd3 activity more severely than MGCA7-linked $_{PARL}$Skd3 subunits. (A) SEC of MGCA7-linked $_{PARL}$Skd3 variants. The three vertical bars represent different molecular weight standards thyroglobulin (669 kDa), ferritin (440 kDa), and ovalbumin (43 kDa) that approximately represent Skd3 dodecamers (grey), hexamers (cyan), or monomers (magenta). **(B)** SEC of SCN-linked $_{PARL}$Skd3 variants. The three vertical bars represent different molecular weight standards thyroglobulin (669 kDa), ferritin (440 kDa), and ovalbumin (43 kDa) that approximately represent Skd3 dodecamers (grey), hexamers (cyan), or

monomers (magenta). **(C)** FRET efficiency after mixing Alexa488-$_{PARL}$Skd3 with buffer, Alexa594-$_{PARL}$Skd3, Alexa594-$_{PARL}$Skd3^{A591V}, or Alexa594-$_{PARL}$Skd3^{R475Q} for 10 min in the presence of ATP (5 mM) at a 1:1 molar ratio with a final labeled $_{PARL}$Skd3 concentration of 1μM. Relative FRET efficiency was compared to WT $_{PARL}$Skd3 using one-way ANOVA and a Dunnett's multiple comparisons test (n = 3, individual data points shown as dots, bars show mean ± SEM, ****p<0.0001). **(D)** FRET efficiency after mixing Alexa488-$_{PARL}$Skd3 with buffer, Alexa594-$_{PARL}$Skd3, Alexa594-$_{PARL}$Skd3^{R408G}, Alexa594-$_{PARL}$Skd3^{N496K}, Alexa594-$_{PARL}$Skd3^{R561G}, or Alexa594-$_{PARL}$Skd3^{R620C} for 10 min in the presence of ATP (5 mM) at a 1:1 molar ratio with a final labelled $_{PARL}$Skd3 concentration of 1μM. Relative FRET efficiency was compared to WT $_{PARL}$Skd3 using one-way ANOVA and a Dunnett's multiple comparisons test (n = 3, individual data points shown as dots, bars show mean ± SEM, **p<0.01, ****p<0.0001). **(E-H)** ATPase activity of $_{PARL}$Skd3 was mixed with various ratios of $_{PARL}$Skd3^{A591V} (E) or $_{PARL}$Skd3^{R620C} (G). ATPase activity was buffer subtracted and normalized to $_{PARL}$Skd3 (n = 3, data shown as black dots with mean ± SEM). Luciferase disaggregase activity of $_{PARL}$Skd3 mixed with various ratios of $_{PARL}$Skd3^{A591V} (F) or $_{PARL}$Skd3^{R620C} (H). Disaggregase activity was buffer subtracted and normalized to $_{PARL}$Skd3 (n = 3, data shown as black dots with mean ± SEM). **(I)** Table summarizing the effect of MGCA7-linked subunits on ATPase activity and luciferase disaggregase activity. **(J)** Table summarizing the effect of SCN-linked subunits on ATPase activity and luciferase disaggregase activity.
Related to Figure 7.

	PARLSkd3 (Class 1,AAA+ only) EMDB 26121 PDB 7TTR	PARLSkd3 (Class 1, AAA+ & ANK) EMDB 26122 PDB 7TTS	PARLSkd3 (Class 2)	PARLSkd3$^{\Delta 1-2}$ (Class 1)
Data collection and processing				
Microscope and camera	Titan Krios, K3			Glacios, K2
Magnification	105,000			45,000
Voltage (kV)	300			200
Data acquisition software	Serial EM			Serial EM
Exposure navigation	Image Shift			Image Shift
Electron exposure (e^- /Å^2)	68			55.8
Final particle images (no.)	358,000		130,000	165,354
Map resolution (Å)	2.96	~6 (filtered)	7.2	7.9
FSC threshold	0.143			
Map resolution range (Å)	2.5-6.5	6	6-10	6-20
Refinement				
Model resolution (Å)	2.9	2.9	-	-
FSC threshold	.143	.143	-	-
Map sharpening *B* factor (Å^2)	-119	-	-497	-610
Model composition				
Non-hydrogen atoms	15,699	18,796	-	-
Protein residues	1926	2700	-	-
Ligands	9	9	-	-
B factors (Å^2)			-	-
Protein	158.16	178.33	-	-
Ligand	54.10	54.10	-	-
R.m.s. deviations				-
Bond lengths (Å)	.011	.010	-	-
Bond angles (°)	1.249	1.222	-	-
Validation				
MolProbity score	1.67	1.53	-	-
Clashscore	6		-	-
Poor rotamers (%)	.30	.30	-	-

Table S1. Cryo-EM data collection, refinement and validation statistics of PARLSkd3 structures.

Related to Figures 1, 2 and 3.